The Astronomical Journal, 144:72 (19pp), 2012 September doi:10.1088/0004-6256/144/3/72

VERY LOW MASS STELLAR AND SUBSTELLAR COMPANIONS TO SOLAR-LIKE STARS FROM MARVELS. II. A SHORT-PERIOD COMPANION ORBITING AN F STAR WITH EVIDENCE OF A STELLAR TERTIARY AND SIGNIFICANT MUTUAL INCLINATION

Scott W. Fleming[1,2,3], Jian Ge[1], Rory Barnes[4], Thomas G. Beatty[5], Justin R. Crepp[6], Nathan De Lee[1,7], Massimiliano Esposito[8,9], Bruno Femenia[8,9], Leticia Ferreira[10,11], Bruce Gary[7], B. Scott Gaudi[5], Luan Ghezzi[11,12], Jonay I. González Hernández[8,9], Leslie Hebb[7], Peng Jiang[1], Brian Lee[1], Ben Nelson[1], Gustavo F. Porto de Mello[10,11], Benjamin J. Shappee[5], Keivan Stassun[7,13], Todd A. Thompson[5], Benjamin M. Tofflemire[4,14], John P. Wisniewski[4], W. Michael Wood-Vasey[15], Eric Agol[4], Carlos Allende Prieto[8,9], Dmitry Bizyaev[16], Howard Brewington[16], Phillip A. Cargile[7], Louis Coban[15], Korena S. Costello[15], Luis N. da Costa[11,12], Melanie L. Good[15], Nelson Hua[15], Stephen R. Kane[17], Gary R. Lander[15], Jian Liu[1], Bo Ma[1], Suvrath Mahadevan[2,3], Marcio A. G. Maia[11,12], Elena Malanushenko[16], Viktor Malanushenko[16], Demitri Muna[18], Duy Cuong Nguyen[1,19], Daniel Oravetz[16], Martin Paegert[7], Kaike Pan[16], Joshua Pepper[7], Rafael Rebolo[8,9,20], Eric J. Roebuck[15], Basilio X. Santiago[11,21], Donald P. Schneider[2,3], Alaina Shelden[16], Audrey Simmons[16], Thirupathi Sivarani[22], Stephanie Snedden[16], Chelsea L. M. Vincent[15], Xiaoke Wan[1], Ji Wang[1], Benjamin A. Weaver[18], Gwendolyn M. Weaver[15], and Bo Zhao[1]

[1] Department of Astronomy, University of Florida, 211 Bryant Space Science Center, Gainesville, FL 2611-2055, USA; scfleming@psu.edu
[2] Department of Astronomy and Astrophysics, The Pennsylvania State University, 525 Davey Laboratory, University Park, PA 16802, USA
[3] Center for Exoplanets and Habitable Worlds, The Pennsylvania State University, University Park, PA 16802, USA
[4] Department of Astronomy, University of Washington, P.O. Box 351580, Seattle, WA 98195, USA
[5] Department of Astronomy, The Ohio State University, 140 West 18th Avenue, Columbus, OH 43210, USA
[6] Department of Astronomy, California Institute of Technology, 1200 E. California Blvd., Pasadena, CA 91125, USA
[7] Department of Physics and Astronomy, Vanderbilt University, Nashville, TN 37235, USA
[8] Instituto de Astrofísica de Canarias (IAC), E-38205 La Laguna, Tenerife, Spain
[9] Departamento de Astrofísica, Universidad de La Laguna, 38206 La Laguna, Tenerife, Spain
[10] Observatório do Valongo, Universidade Federal do Rio de Janeiro, Ladeira do Pedro Antônio, 43, CEP: 20080-090, Rio de Janeiro, RJ, Brazil
[11] Laboratório Interinstitucional de e-Astronomia, LIneA, Rua Gal. José Cristino 77, Rio de Janeiro, RJ-20921-400, Brazil
[12] Observatório Nacional, Rua General José Cristino, 77, 20921-400 São Cristóvão, Rio de Janeiro, RJ, Brazil
[13] Department of Physics, Fisk University, 1000 17th Ave. N., Nashville, TN 37208, USA
[14] Astronomy Department, University of Wisconsin-Madison, 475 N Charter St, Madison, WI 53706, USA
[15] Department of Physics and Astronomy, University of Pittsburgh, Pittsburgh, PA 15260, USA
[16] Apache Point Observatory, P.O. Box 59, Sunspot, NM 88349-0059, USA
[17] NASA Exoplanet Science Institute, Caltech, MS 100-22, 770 South Wilson Avenue, Pasadena, CA 91125, USA
[18] Center for Cosmology and Particle Physics, New York University, New York, NY 10003, USA
[19] Department of Physics and Astronomy, University of Rochester, Rochester, NY 14627, USA
[20] Consejo Superior de Investigaciones Científicas, Calle Serrano 117, E-28006 La Laguna, Spain
[21] Instituto de Física, UFRGS, Caixa Postal 15051, Porto Alegre, RS-91501-970, Brazil
[22] Indian Institute of Astrophysics, 2nd block, Koramangala, Bangalore 560034, India
Received 2012 April 19; accepted 2012 June 22; published 2012 July 27

ABSTRACT

We report the discovery via radial velocity (RV) measurements of a short-period ($P = 2.430420 \pm 0.000006$ days) companion to the F-type main-sequence star TYC 2930-00872-1. A long-term trend in the RV data also suggests the presence of a tertiary stellar companion with $P > 2000$ days. High-resolution spectroscopy of the host star yields $T_{\rm eff} = 6427 \pm 33$ K, $\log g = 4.52 \pm 0.14$, and [Fe/H] $= -0.04 \pm 0.05$. These parameters, combined with the broadband spectral energy distribution (SED) and a parallax, allow us to infer a mass and radius of the host star of $M_1 = 1.21 \pm 0.08\ M_\odot$ and $R_1 = 1.09^{+0.15}_{-0.13}\ R_\odot$. The minimum mass of the inner companion is below the hydrogen-burning limit; however, the true mass is likely to be substantially higher. We are able to exclude transits of the inner companion with high confidence. Further, the host star spectrum exhibits a clear signature of Ca H and K core emission, indicating stellar activity, but a lack of photometric variability and small $v \sin I$ suggest that the primary's spin axis is oriented in a pole-on configuration. The rotational period of the primary estimated through an activity–rotation relation matches the orbital period of the inner companion to within $1.5\,\sigma$, suggesting that the primary and inner companion are tidally locked. If the inner companion's orbital angular momentum vector is aligned with the stellar spin axis as expected through tidal evolution, then it has a stellar mass of ~0.3–0.4 $M_\odot$. Direct imaging limits the existence of stellar companions to projected separations <30 AU. No set of spectral lines and no significant flux contribution to the SED from either companion are detected, which places individual upper mass limits of $M_{\{2,3\}} \lesssim 1.0\ M_\odot$, provided they are not stellar remnants. If the tertiary is not a stellar remnant, then it likely has a mass of ~0.5–0.6 $M_\odot$, and its orbit is likely significantly inclined from that of the secondary, suggesting that the Kozai–Lidov mechanism may have driven the dynamical evolution of this system.

Key words: binaries: close – binaries: spectroscopic – stars: individual (TYC 2930-00872-1)

Online-only material: color figures

1. INTRODUCTION

Exoplanet surveys have contributed to a wide range of ancillary astrophysical disciplines during the last two decades, including studies of variable stars, binary stars, and brown dwarf (BD) companions. During the course of operation, these surveys detect a large variety of stellar binaries that can be used to study stellar structure, atmospheres, and formation mechanisms. One example of the latter is a study of the multiplicity of close binaries, e.g., the fraction of close binaries that are in triple or higher-order systems. Indeed, triple systems are not uncommon among short-period binaries; 9 out of 16 binaries with $P < 100$ days in the volume-limited sample of Raghavan et al. (2010) are members of triple systems. Shorter-period binaries have an even greater probability of being in a multiple-star system ($\sim 80\%$ for $P < 7$ days versus $\sim 40\%$ for $P > 7$ days; Tokovinin et al. 2006).

The orbital elements of such binaries, including the mutual inclinations of the companions' orbital angular momentum vectors, are fossil records of their formation process, and provide critical constraints to binary star formation models (Sterzik & Tokovinin 2002). Comparison of the orbital and physical properties between different binary hierarchies also provides insight into binary star formation theory (Tokovinin 2008). In fact, the dynamical evolution of these systems may be dominated by dynamical interactions between the inner and outer companions via a combination of the Kozai–Lidov mechanism (Kozai 1962; Lidov 1962) and tidal forces, which drive the inner companion to shorter orbital separations until it circularizes with some period $P \lesssim 10$ days, beyond which tidal forces are ineffective (Fabrycky & Tremaine 2007).

In this paper, we present the discovery of a companion with a substellar minimum mass orbiting the bright ($V = 9.8$) F-type star TYC 2930-00872-1 (Høg et al. 2000, hereafter TYC 2930), with an orbital period of $P = 2.430420 \pm 0.000006$ days. This discovery is part of a series of papers dedicated to analyses of individual low-mass companions in anticipation of a global analysis of the MARVELS (Multi-object APO Radial Velocity Exoplanets Large-area Survey) sample at the conclusion of the survey (e.g., Lee et al. 2011; Wisniewski et al. 2012); therefore, TYC 2930 is also designated "MARVELS-2" as an internal reference within this series. The a priori transit probability of the inner companion is $\sim 13\%$ with an expected central transit depth of $\sim 0.9\% \pm 0.25\%$ for a 1 $R_{\rm Jup}$ companion radius, although no transits are detected. An additional, long-term trend in the radial velocity (RV) data is detected from a stellar tertiary in the system. A detailed analysis of the combined RV, spectroscopic, and photometric data suggests the inner companion is oriented toward a pole-on configuration and is more likely an M dwarf with a mass ~ 0.3–$0.4\ M_{\odot}$, while the tertiary is likely to be less inclined. In such a scenario, the mutual inclination between the secondary and tertiary is likely to be significant, which would make this an excellent example of a system whose dynamical history was driven via the Kozai–Lidov mechanism.

The paper is organized such that Section 2.1 describes the spectroscopic observations and their data processing, Section 2.2 describes the archival and observed photometry for the system, Section 3 describes the characterization of the host star's properties, including mass, radius, effective temperature, surface gravity, metallicity, stellar activity, and rotation rate, Section 4 describes our determination of the orbital parameters from fitting the measured RVs, Section 5 describes both Lucky Imaging and adaptive optics (AO) imaging to search for any wide companions to TYC 2930, Section 6 describes our search for photometric variability and any potential transits of the inner companion, Section 7 discusses the tidal evolution of the inner companion, Section 8 describes the posterior distribution of the true masses for both the secondary and tertiary given the results from the previous sections, and finally, Section 9 investigates the possible dynamical history of the system via the Kozai–Lidov mechanism.

2. DESCRIPTION OF OBSERVATIONS

2.1. Spectroscopic Observations

MARVELS (Ge et al. 2008) is part of the Sloan Digital Sky Survey III (SDSS-III; Eisenstein et al. 2011). The instrument uses dispersed fixed-delay interferometry (Ge et al. 2002; Ge 2002; Erskine 2002; Erskine et al. 2003; van Eyken et al. 2011; Wang et al. 2012) on the 2.5 m SDSS telescope (Gunn et al. 2006) at Apache Point Observatory (APO) to measure precision radial velocities of 60 stars simultaneously. Both beams of the interferometer are imaged onto the detector for a given star, for a total of 120 spectra, producing two simultaneous RV measurements for each star from beams that travel through a slightly different instrument path. The survey began in the fall of 2008 and will ultimately target several thousand stars between $7.6 < V < 12$, with a baseline goal of <30 m s^{-1} precision for the faintest stars. Each star is observed $\sim$20–30 times over a typical baseline of 1.75 years. In addition to exoplanets, the survey will conduct studies of stellar atmospheres, binary stars, and rare companions such as BDs and very low mass ($M \lesssim 150\ M_{\rm Jup}$) stars at short orbital periods.

TYC 2930 was observed a total of 33 times over a baseline of 707 days. The data were processed by the MARVELS pipeline following the steps described in Lee et al. (2011). The resultant RV measurements from both interferometer output beams were combined via a weighted average after they were found to agree to within the measurement errors. The formal mean RV precision was 23 m s^{-1}. Following Fleming et al. (2010), the RV uncertainties for this star were further scaled by a "quality factor" QF = 6.69, a first-order correction used to partially account for residual systematic errors. For each of the other 118 spectra in this field, an individual QF is calculated as the RV rms about the mean, divided by the median formal RV uncertainty for that star. On average, most of the MARVELS targets in a given field should be RV stable at the level of tens of m s^{-1}, and therefore should have QF $\sim$ 1. Since the average QF across the plate is significantly larger, we treat that as one measurement of the residual uncertainties from the pipeline-produced RVs. The dates and RVs from the MARVELS observations are presented in Table 1.

Additional RV observations were conducted using the Spettrografo Alta Risoluzione Galileo (SARG) spectrograph (Gratton et al. 2001) on the 3.58 m Telescopio Nazionale Galileo (TNG) telescope. The data were obtained using the yellow grism with a slit of $0\farcs8 \times 5\farcs3$ on-sky that produces a resolving power of $R = 57,000$ over the wavelength range $462 < \lambda < 792$ nm. A total of 20 observations were taken, spanning $\sim$408 days, using an iodine cell that serves as an RV calibration source. The average signal-to-noise ratio per resolution element, averaged across the central 200 pixels of all the orders, ranges from 150 to 290. An additional observation was taken without the iodine cell to be used as a stellar template and to derive stellar parameters. The signal-to-noise ratio per resolution element of the template spectrum is $\sim$400 at 607 nm.

Table 1
MARVELS RV—TYC 2930

HJD_{UTC}	RV (km s^{-1})	QF-scaled σ_{RV} (km s^{-1})
2454843.86946	2.571	0.129
2454844.82593	−8.036	0.099
2454845.83333	−6.326	0.095
2454846.82454	1.039	0.077
2454847.77335	−13.549	0.083
2454866.71528	−7.996	0.087
2454874.74327	−10.879	0.118
2454876.77555	−12.778	0.128
2455135.87308	9.021	0.120
2455136.84418	−7.602	0.105
2455137.85985	7.069	0.165
2455138.88972	−1.846	0.120
2455139.78368	−3.523	0.110
2455139.96991	0.506	0.099
2455143.86472	−4.111	0.102
2455144.86232	1.319	0.084
2455145.86470	5.141	0.107
2455171.89913	7.588	0.094
2455172.85712	−0.125	0.118
2455200.91808	5.337	0.077
2455254.77584	10.438	0.085
2455258.75174	−4.726	0.104
2455281.65360	10.108	0.141
2455466.86921	1.955	0.137
2455466.91135	0.996	0.105
2455487.84516	7.664	0.077
2455488.86530	−0.942	0.101
2455489.87545	−0.646	0.095
2455494.90526	3.061	0.099
2455500.90889	1.409	0.092
2455521.82966	6.852	0.107
2455522.85494	−0.199	0.117
2455550.88590	4.448	0.195

The SARG data are processed using the standard IRAF Echelle reduction packages. Frames are trimmed, bias subtracted, flat-field corrected, aperture traced, and extracted. ThAr lines are used to calibrate the wavelength solution. The RVs are measured using the iodine cell technique (Marcy & Butler 1992). The 21 SARG orders that have sufficiently strong iodine lines lie in the wavelength range $504 < \lambda < 611$ nm. Each order is subdivided into 10 sections from which an RV is measured. The resulting 210 RV measurements are then 2σ clipped using three iterations. The remaining N RV measurements are averaged to produce a single RV measurement. The RV uncertainty is given by $\sigma_{RV} = \sigma N^{-1/2}$, where σ is the dispersion of the points after the 2σ clipping. Table 2 contains the dates and RVs from the SARG observations.

A high signal-to-noise ratio spectrum of TYC 2930 was obtained with the ARC Echelle Spectrograph (ARCES; Wang et al. 2003) on the APO 3.5 m telescope for the purposes of stellar characterization. The spectrograph delivers $R \sim 31{,}500$ spectra spanning a wavelength range $320 < \lambda < 1000$ nm on a single 2048 × 2048 SITe CCD. The spectra were reduced using an IRAF script that corrects for bias and dark current subtraction, cosmic rays, and bad pixels. Flat fielding is performed using a combination of quartz lamp exposures with and without a blue filter, while a ThAr lamp is used for wavelength calibration. A single integration of 900 s was taken, yielding a spectrum with a signal-to-noise ratio of ∼220 per resolution element at 607 nm.

Table 2
SARG RV—TYC 2930

HJD_{UTC}	RV (km s^{-1})	σ_{RV} (km s^{-1})
2455436.71196	2.568	0.026
2455460.73287	−3.624	0.015
2455460.74384	−3.400	0.018
2455460.75505	−3.196	0.021
2455495.57813	5.964	0.034
2455495.61314	5.550	0.020
2455495.69113	4.642	0.024
2455495.71406	4.247	0.023
2455516.55620	−5.453	0.022
2455516.63469	−3.758	0.012
2455553.50056	4.252	0.014
2455553.66834	5.920	0.013
2455580.42134	5.869	0.012
2455580.46981	6.010	0.012
2455580.59158	5.770	0.014
2455666.42077	−8.355	0.014
2455698.35676	−12.133	0.016
2455791.70794	3.088	0.012
2455844.61269	−8.335	0.015
2455844.74543	−5.583	0.012

Long-term, queue-scheduled (Shetrone et al. 2007), RV monitoring of the TYC 2930 system has been initiated using the High Resolution Spectrograph (Tull 1998) on the Hobby–Eberly Telescope (Ramsey et al. 1998) to further characterize the orbit of the suspected long-period companion. These RVs are expected to be presented in a separate paper at the conclusion of that project.

2.2. Photometry Observations

Photometry of TYC 2930 was performed using the Hereford Arizona Observatory (HAO), a private observatory in southern Arizona (observatory code G95 in the IAU Minor Planet Center). Observations were taken in Johnson B and V filters using a Meade 14 inch LX200GPS telescope and a 2184 × 1472 pixel SBIG ST-10XME CCD. Landolt standard stars (Landolt & Uomoto 2007; Landolt 2009) were observed in the Kapteyn Selected Area 98 (SA 98) for calibration. A photometric precision of 0.023 mag was obtained in B and 0.018 in V. The measured fluxes and uncertainties are presented in Table 3.

We obtained relative photometric time series from several ground-based telescopes (SuperWASP, Allegheny Observatory, KELT-North) to search for transits and examine the photometric stability of the primary star. We briefly describe each of these data sets in turn. The SuperWASP instruments measure fluxes of millions of stars via wide-angle images of the night sky using a broadband filter that covers 400–700 nm and are described in Pollacco et al. (2006). For TYC 2930, a total of 2204 observations from 2006 and 1309 observations from 2007 are extracted from the SuperWASP public archive.[23]

We obtained photometric observations on seven nights in February and March of 2011 using the Keeler 16 inch Meade RCS-400 telescope at Allegheny Observatory. The CCD detector is a 3060 × 2040 pixel SBIG KAF-6303/LE with a 0.″57 per pixel scale, and all observations were taken through a Johnson–Cousins R filter. Typical seeing was 2.″5 with integration times ranging from 20 to 30 s. The images were processed

[23] http://www.wasp.le.ac.uk/public/

Table 3
Stellar Properties—TYC 2930

Parameter	Value	$\pm 1\sigma$
α_{J2000} (deg)[a]	93.880921	0.000004
δ_{J2000} (deg)[a]	+39.931826	0.000005
FUV[b]	19.815	0.195
NUV[b]	14.34	0.01
B (HAO)	10.365	0.023
V (HAO)	9.842	0.018
J (2MASS)	8.770	0.029
H (2MASS)	8.539	0.047
K_S (2MASS)	8.458	0.023
WISE 3.4 μm	8.380	0.024
WISE 4.6 μm	8.392	0.023
WISE 12 μm	8.329	0.029
WISE 22 μm	8.201	0.245
μ_α(mas yr^{-1})[c]	3.42	2.05
μ_δ(mas yr^{-1})[c]	−46.69	1.13
Parallax Π(mas)[c]	7.15	1.51
A_V (SED)	0.33	0.06
$T_{\rm eff}$(K)	6427	33
log (g[cm s^{-1}])	4.52	0.14
[Fe/H]	−0.04	0.05
ξ_t(km s^{-1})	1.40	0.05
$v \sin I$(km s^{-1})	3.8	$^{+1.9}_{-2.8}$
M_* ($M_\odot$)	1.21	0.08
R_* ($R_\odot$)	1.09	$^{+0.15}_{-0.13}$
RPM$_J$	2.14	...

Notes.
[a] Tycho-2 Catalog (Høg et al. 2000).
[b] *GALEX* (Martin et al. 2005).
[c] van Leeuwen (2007).

using standard bias, dark, and flat-field calibration images taken on the same nights. Astrometric solutions were computed based on the positions of stars in the 20′ × 30′ field of view from the Two Micron All Sky Survey (2MASS) Point-Source Catalog (Skrutskie et al. 2006). After image calibration, we performed circular aperture photometry with a 10 pixel radius (5.″7 on sky) and estimated the local sky background from a 15–20 pixel annulus around each star. Relative photometry was determined by comparing the measured flux from TYC 2930 with two nearby stars.

We also extracted photometric time-series data of TYC 2930 obtained by the Kilodegree Extremely Little Telescope (KELT) North transit survey (Pepper et al. 2007; Siverd et al. 2009). KELT uses a red-pass filter with a 50% transmission point at 490 nm, which, when folded with the CCD response, yields an effective bandpass similar to R, but broader. The standard KELT data reduction procedure uses the ISIS image subtraction package (Alard & Lupton 1998), combined with point-spread fitting photometry using DAOPHOT (Stetson 1987).

In the case of TYC 2930, the standard KELT data reduction procedure yielded an unusable light curve due to the presence of the nearby bright star HD 42903, which was partially saturated in the KELT images. We correct the systematics by performing simple aperture photometry on both TYC 2930 and HD 42903 using the subtracted images. We used two apertures centered on HD 42903, and one aperture centered on TYC 2930. We sized the apertures around HD 42903 such that they formed an annulus that included the systematic artifacts. The single aperture around TYC 2930, in the middle of the artifact, had the same diameter as the width of the annulus around HD 42903. By subtracting the summed flux in the aperture around TYC 2930 from the annulus around HD 42903, we are left with the average negative flux value in the artifact for each of the subtracted images. We then used this average value to correct the results from the aperture around TYC 2930. This procedure was tested using known variable stars and on stars with similar brightness ratios and angular separations to confirm that accurate results were obtained and no intrinsic variations were suppressed.

Table 4
IAC and BPG Stellar Parameters

Parameter	IAC		BPG	
	SARG	ARCES	SARG	ARCES
Fe I lines used	173	172	60	67
Fe II lines used	21	25	8	9
$T_{\rm eff}$(K)	6456 ± 49	6413 ± 41	6406 ± 110	6415 ± 76
log (g[cm s^{-1}])	4.68 ± 0.27	4.53 ± 0.21	4.47 ± 0.26	4.44 ± 0.21
[Fe/H]	−0.02 ± 0.09	−0.01 ± 0.07	−0.13 ± 0.10	−0.03 ± 0.07
ξ_t(km s^{-1})	1.296 ± 0.076	1.464 ± 0.059	1.44 ± 0.20	1.34 ± 0.12

3. STELLAR CHARACTERIZATION

3.1. Stellar Parameters

TYC 2930 (HIP 29714) is a bright F-type star located 6.′16 from the center of the open cluster NGC 2192. The *Hipparcos* parallax measurement (van Leeuwen 2007) places the star at a distance of $d = 140 \pm 29.5$ pc. The RPM–J (Collier Cameron et al. 2007) value of 2.14 and $(J - H)$ color of 0.23 are consistent with a main-sequence star. We further characterize the host star's properties using the SARG template spectrum and the ARCES spectrum by measuring equivalent widths of Fe I and Fe II lines. We utilize two independent pipelines that derive stellar atmospheric parameters based on the Fe I and Fe II excitation and ionization equilibria. We refer to these different pipelines as the "IAC" (Instituto de Astrofísica de Canarias) and "BPG" (Brazilian Participation Group) pipelines, which are described in detail by Wisniewski et al. (2012). We apply both these analyses to the SARG and ARCES spectra, and find spectroscopic parameters that are consistent across both groups and both instruments. We summarize the individual $T_{\rm eff}$, log (g), [Fe/H], and ξ_t in Table 4.

A final, mean value for each parameter is calculated following Wisniewski et al. (2012), yielding $T_{\rm eff} = 6427 \pm 33$ K, log (g) $= 4.52 \pm 0.14$, [Fe/H] $= -0.04 \pm 0.05$, and $\xi_t = 1.40 \pm 0.05$ km s^{-1}. We note that while there can be correlations between the measured stellar parameters, we treat their uncertainties as independent and Gaussian distributed in this analysis. Estimates of the primary's mass and radius are determined using a Markov Chain Monte Carlo (MCMC) analysis applied to the empirical relationship of Torres et al. (2010), the *Hipparcos* parallax, and the stellar parameters described above. The uncertainties for the mass and radius include the correlations of the best-fit coefficients from Torres et al. (2010) and the reported scatter in that relation ($\sigma_{\log m} = 0.027$ and $\sigma_{\log r} = 0.014$). The radius of the primary is $R = 1.09^{+0.15}_{-0.13}\ R_\odot$ and the mass is $M = 1.21 \pm 0.08\ M_\odot$. All of the stellar parameters are summarized in Table 3.

3.2. Rotation Rate, SED Fitting, and Stellar Activity

We measure the stellar rotational velocity $v \sin I$ from the SARG template spectrum. Note that we utilize a notation that

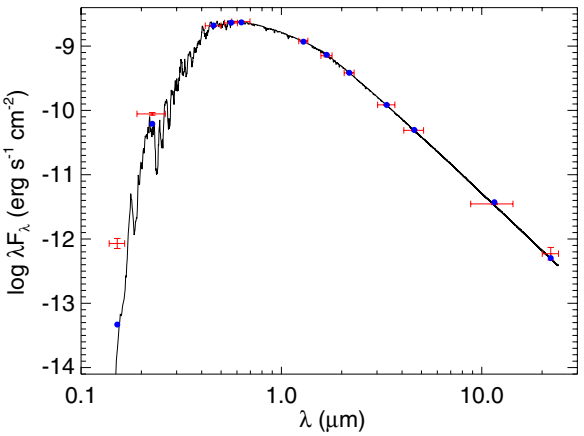

Figure 1. NextGen model (solid line) compared to the observed broadband fluxes of the host star. Blue points represent the expected fluxes in each band based on the model, red horizontal bars are the approximate bandpass widths, and red vertical bars are the flux uncertainties. The $T_{\rm eff}$, log (g), and [Fe/H] are fixed at the spectroscopically determined values, while $A_{\rm V}$ is allowed to float. No evidence of IR excess is detected, while there is potentially some *GALEX* FUV excess indicating elevated levels of stellar activity.

(A color version of this figure is available in the online journal.)

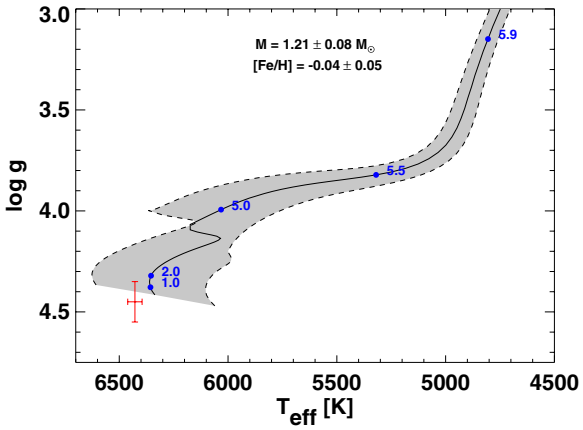

Figure 2. H-R diagram based on Yonsei–Yale stellar evolution models (Demarque et al. 2004). The solid track is for the best-fit stellar parameters, while the two dashed tracks represent the 1σ uncertainties. The blue dots represent star ages in Gyr. TYC 2930 (red point) appears to lie on the main sequence.

(A color version of this figure is available in the online journal.)

distinguishes I (the angle between our line of sight and the stellar rotation axis) from i (the angle between our line of sight and a companion's orbital angular momentum vector). We use an interpolated Kurucz model spectrum (Kurucz 1993) using the spectroscopically determined $T_{\rm eff}$, log (g), and [Fe/H] convolved to the instrumental profile (FWHM of 5.3 km s^{-1}). Testing showed that macroturbulence (ζ_t) had only a marginal affect on the final result, so we adopt values ranging from 2 to 5 km s^{-1}. The model spectra are broadened with a Gray's profile over a range of $v \sin I$ from 0 to 10 km s^{-1}. These models are then compared via a χ^2 analysis with the observed spectrum, which yields $v \sin I = 3.8(+1.9, -2.8)$ km s^{-1}, effectively placing an upper limit of $v \sin I \lesssim 6$ km s^{-1}.

We construct a spectral energy distribution (SED) using fluxes from *GALEX* (Martin et al. 2005), the HAO observations, the 2MASS (Skrutskie et al. 2006) Point-Source Catalog, and the four *Wide-field Infrared Survey Explorer* (*WISE*; Wright et al. 2010) bands. NextGen models from Hauschildt et al. (1999) are used to construct theoretical SEDs by fixing $T_{\rm eff}$, log (g), and [Fe/H] at the spectroscopic values, while the extinction $A_{\rm V}$ is constrained to a maximum value of $A_{\rm V} = 0.6$ based on the reddening maps of Schlegel et al. (1998) for galactic coordinates $(l, b) = (173.^\circ365948, 10.^\circ729936)$. Figure 1 shows the best-fit model, which has a χ^2/degrees of freedom (dof) = 1.2, $A_{\rm V} = 0.33 \pm 0.06$, no evidence for IR excess, and some excess in the *GALEX* FUV band. Figure 2 places the star on an H-R diagram based on Yonsei–Yale stellar models (Demarque et al. 2004), indicating that TYC 2930 is consistent with an F-type dwarf with an age $t < 2$ Gyr.

To further explore the FUV excess, Figure 3 compares the ARCES spectrum of TYC 2930, centered on the Ca II K line at 393.37 nm, with archival Fibre-fed Extended Range Optical Spectrograph (FEROS; Kaufer et al. 1999) spectra of the standard stars HD 43042, HD 142, and HD 120136 from Ghezzi et al. (2010). FEROS is an $R \sim 48{,}000$ spectrograph with a wavelength range of $350 < \lambda < 920$ nm and high throughput (~20%). There is clear Ca K core emission from TYC 2930 indicating significant chromospheric activity. We measure the S index (Vaughan et al. 1978; Vaughan & Preston 1980; Duncan et al. 1991) from the APO spectrum and convert to $R'_{\rm HK}$, finding a log $R'_{\rm HK} = -4.44 \pm 0.05$.

4. ORBITAL ANALYSIS AND COMPANION MINIMUM MASS

4.1. Radial Velocity Fitting

The MARVELS RVs show evidence of a long-term, positive linear trend indicating a possible tertiary object. The TNG data also showed evidence of a long-term trend, but with a negative slope. Fitting the MARVELS+SARG data with a single-companion model combined with non-Keplerian trends (linear, parabolic, and cubic) yielded residuals with significant systematics, suggesting a two-companion Keplerian model is required.

The combined RVs were initially fit using the RVLIN package (Wright & Howard 2009) for the purpose of obtaining initial values of the orbital parameters. Uncertainties are calculated later using MCMC analysis. The initial best-fit orbital period for the inner companion is $P_2 = 2.430420$ days, with a semiamplitude $K_2 = 8724$ m s^{-1}, and an eccentricity that is consistent with a circular orbit. Figure 4 shows the MARVELS (blue) and SARG (red) RVs phase folded on the best-fit orbital solution for this inner companion after removing the effects of the longer period orbit. The bottom panel plots the residual RVs after removing the shorter period orbit. The unfolded RVs from MARVELS (blue) and SARG (red) are shown in Figure 5, where the shorter period orbit has been removed and the best-fit model of the longer period orbit is plotted as the solid line. The residuals of the combined, two-companion solution are shown in the bottom panel.

To derive final orbital parameters and associated uncertainties, we perform an MCMC analysis closely following the methods of Ford (2006). For review, our goal is to estimate the uncertainties in our set of model parameters, $\theta = \{P_2, P_3, K_2, K_3, e_2, e_3, \omega_2, \omega_3, T_{P2}, T_{P3}, \gamma_{\rm off}, \gamma_{0,\rm inst}\}$, where P is the orbital period, K is the RV semiamplitude, e is the orbital eccentricity, ω is the argument of periastron, T_p is the epoch of periastron, $\gamma_{\rm off}$ is the offset between the two sets of instruments, $\gamma_{0,\rm inst}$ is the (instrumental) systemic velocity, and the subscripts $j = \{2, 3\}$ refer to the shorter period and longer period companions, respectively. We sample the posterior probability distribution given

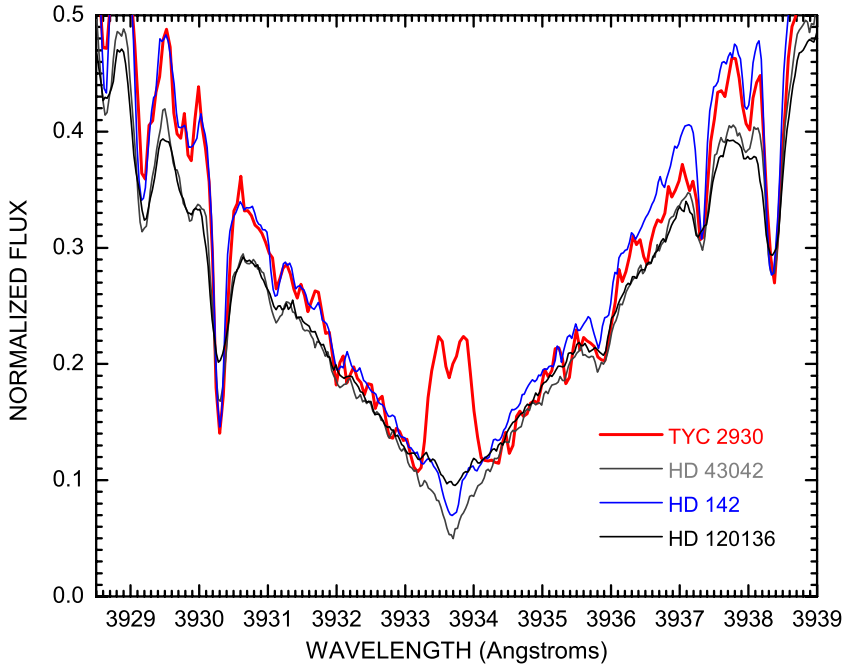

Figure 3. Ca II K line of TYC 2930 compared to standard stars. TYC 2930 has clear core emission indicating that the host star is active compared to other stars with similar stellar parameters.

(A color version of this figure is available in the online journal.)

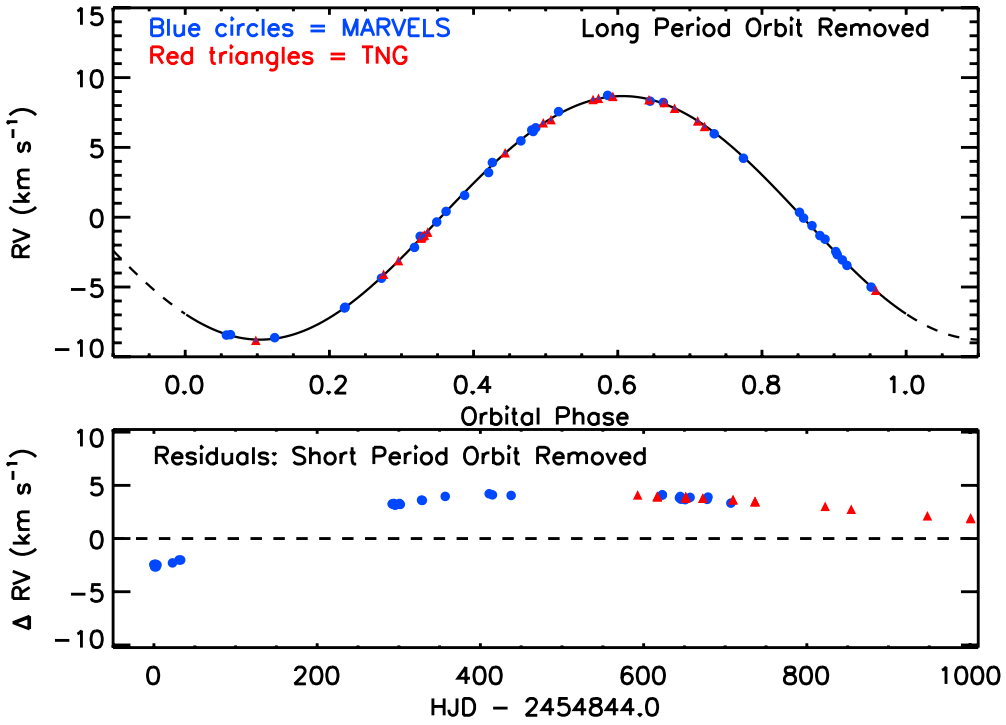

Figure 4. Phase-folded MARVELS (blue) and SARG (red) RVs of MARVELS-2b. The orbit of the long-period companion and the systemic velocity ($\gamma_{0,\mathrm{inst}} = -6.642\,\mathrm{km\,s^{-1}}$) have been removed in the top panel. The bottom panel shows the residual RVs after removing the short-period companion's orbit and systemic velocity. The RV uncertainties are not visible at this scale.

(A color version of this figure is available in the online journal.)

by Bayes' theorem, where specifics on the priors and likelihood function can be found in Section 3 of Zakamska et al. (2011). To help accelerate convergence, we use additional combinations of parameters identified in Section 4 of Ford (2006). We do not attempt to place constraints on stellar jitter in our model.

We test for non-convergence by monitoring the Gelman–Rubin statistic (Gelman et al. 2003), verifying that it is less than 1.02 for each of the parameters, and that chains have been allowed to run long enough to enter these regions of parameter space at least 100 times. The orbital parameters and 1σ equivalent confidence levels for the inner companion

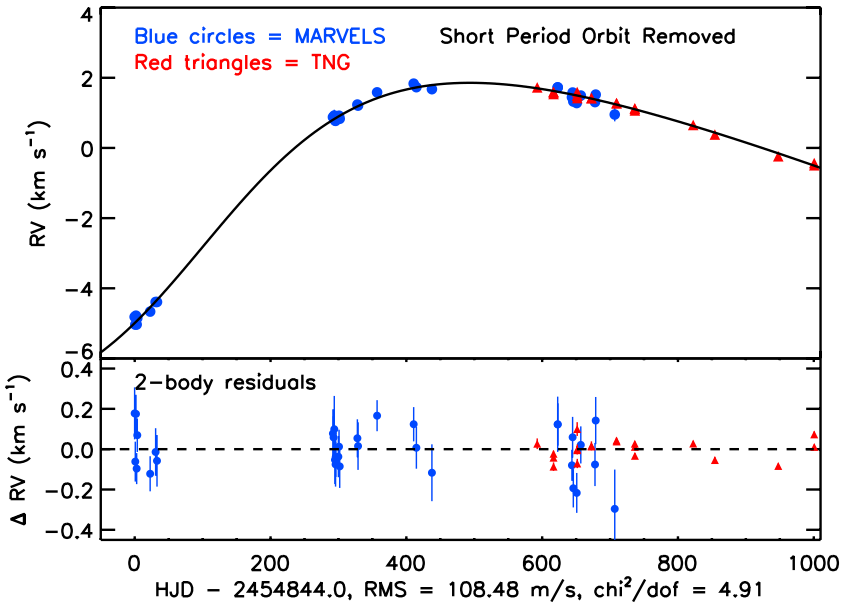

Figure 5. Unfolded MARVELS (blue) and SARG (red) RVs after removing the short-period companion's orbit and the systemic velocity ($\gamma_{0,\rm inst} = -6.642\,{\rm km\,s^{-1}}$). The best-fit model of the outer companion is overplotted as the black line. The residuals of the combined, two-companion model are shown in the bottom panel.
(A color version of this figure is available in the online journal.)

Table 5
Orbital Parameters for the Inner Companion

Parameter	Median	σ (Low)	σ (High)
P (days)	2.430420	0.000006	0.000006
K (km s^{-1})	8.723	0.009	0.009
T_c(HJD$_{\rm UTC}$ − 2,450,000.0)	4842.2640	0.00187	0.00187
e	0.0066	0.0010	0.0010
141.948 ω	142	7	7
$\gamma_{0,\rm inst}$(km s^{-1})	−6.642	2.106	0.904
$\gamma_{\rm off}$(km s^{-1})	−2.890	2.102	0.900
γ_0(km s^{-1})	35.751	0.285	0.285

are given in Table 5. The outer companion's orbital parameters are not well determined, since the orbital period is longer than the baseline of the measurements, but we place a lower limit of $P_3 \gtrsim 2000$ days. The RV semiamplitude and eccentricity of the outer companion are positively correlated with the best-fit orbital period, which must be accounted for when constraining the outer companion's properties.

To place the RVs on an absolute scale, SARG spectra from 620 to 800 nm are cross-correlated with a high-resolution solar spectrum. To partially account for temporal variation in the slit illumination and wavelength solution, a correction is applied via cross-correlation of the telluric lines near 690 nm with a numerical mask. The telluric line locations are taken from Griffin & Griffin (1973); the corrections are typically a few hundred m s^{-1}. After removing the barycentric velocity and orbital motion of the companions based on the MCMC parameters, we find a median absolute RV of $\gamma_0 = 35.751 \pm 0.285\,{\rm km\,s^{-1}}$, where the uncertainty is taken as the rms about the median.

The $\{U, V, W\}$ space velocities can then be calculated using the absolute RV along with the parallax and proper motion measurements from *Hipparcos* (van Leeuwen 2007). We find $\{U, V, W\} = \{-31.2 \pm 0.7, -7.4 \pm 3.1, 3.0 \pm 1.6\}\,{\rm km\,s^{-1}}$, where U is pointing toward the Galactic center. From the classification scheme of Bensby et al. (2003), TYC 2930 is almost certainly a member of the thin disk, as its relative probability of being a thick disk member is just 0.71% ± 0.02%.

4.2. Mass Functions of the Secondary and Tertiary

Using the MCMC chain from the joint RV fit, we can derive the mass functions M_j of companion $j = 2, 3$,

$$\mathcal{M}_j \equiv \frac{(M_j \sin i_j)^3}{(M_1 + M_j)^2} = K_j^3 (1 - e_j^2)^{3/2} \frac{P_j}{2\pi G}. \quad (1)$$

The mass functions are the only properties of the companions that we can derive that are independent of the properties of the primary. For the secondary, we find,

$$\mathcal{M}_2 = (1.6711 \pm 0.0050) \times 10^{-4}\ M_\odot, \quad (2)$$

where the uncertainty is essentially dominated by the uncertainty in K_2, such that $\sigma_{\mathcal{M}_2}/\mathcal{M}_2 \sim 3(\sigma_{K_2}/K_2) = 3 \times 0.1\% \sim 0.3\%$.

For the tertiary, the uncertainty in the mass function is much larger, because of the incomplete phase coverage of the RV curve (Figures 4 and 5). In particular, there is a broad tail toward high mass functions. We therefore quote the median and 68% confidence interval,

$$\mathcal{M}_3 = 2.55^{+5.50}_{-1.22} \times 10^{-2}\ M_\odot. \quad (3)$$

4.3. Minimum Mass and Mass Ratio

To determine the mass or mass ratio of the secondary and tertiary, we must estimate the mass of the primary, as well as the inclination of the secondary and tertiary. To estimate the mass and radius of the primary, we use an MCMC chain where, for each link in the MCMC chain from the joint RV fit, we draw a value of $T_{\rm eff}$, $\log g$, and [Fe/H] for the primary from Gaussian distributions, with means and dispersions given in Table 3. We then use the Torres et al. (2010) relations to estimate the mass M_1 and radius R_1 of the primary, including the intrinsic scatter in these relations.

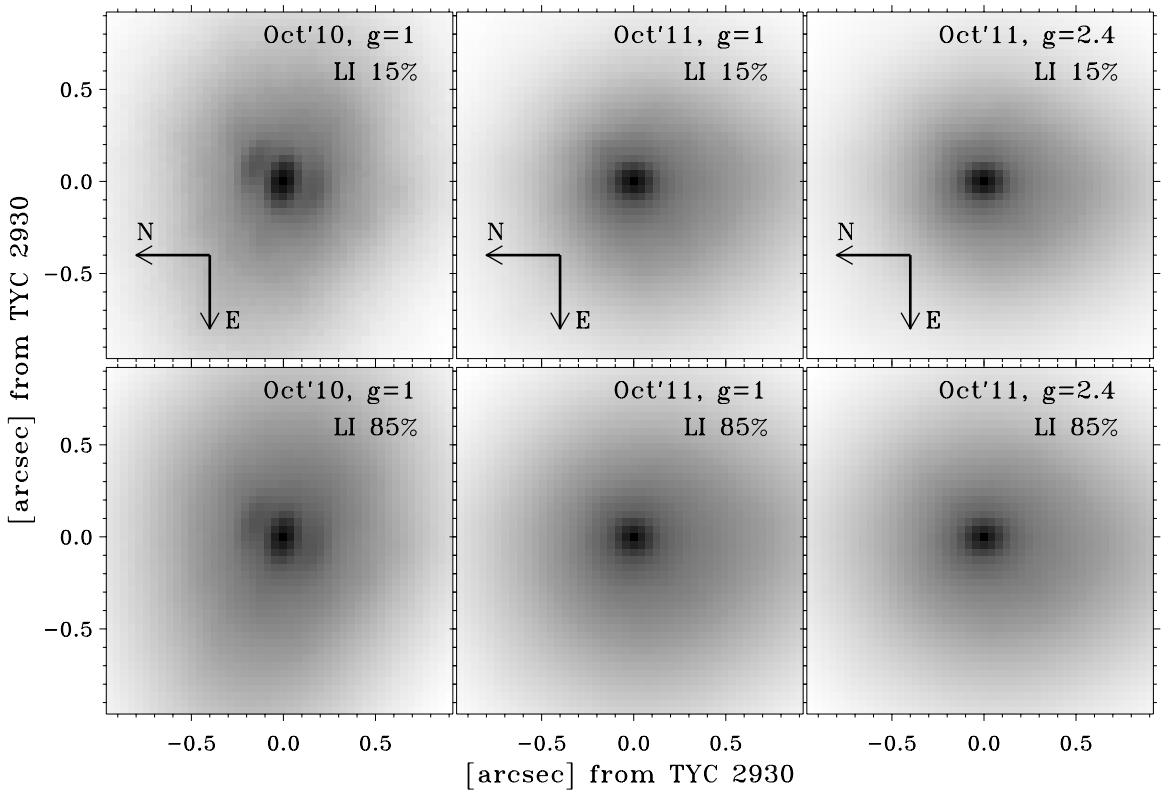

Figure 6. Lucky images of TYC 2930 using the best 15% and 85% of the frames for the 2010 and 2011 observations. The CCD gain, which changed during the 2011 observations, is labeled by *g* in the images. No tertiary companion is detected.

The minimum mass (i.e., M_2 if $\sin i_2 = 1$) and minimum mass ratio of the secondary are

$$M_{2,\min} = 68.1 \pm 3.0\, M_{\rm Jup} = 0.0650 \pm 0.0029\, M_\odot,$$
$$q_2 = 0.0535 \pm 0.0012. \quad (4)$$

The uncertainties in these estimates are almost entirely explained by the uncertainties in the mass of the primary: $\sigma_{M_2}/M_2 \sim (2/3)(\sigma_{M_1}/M_1) = (2/3) \times 6.7\% \sim 4.5\%$, almost exactly the uncertainty in $M_{2,\min}$ above (4.4%), and $\sigma_q/q \sim (1/3)(\sigma_{M_1}/M_1) \sim (1/3) \times 6.7\% \sim 2.3\%$, the uncertainty in q (2.3%). As we show in Section 6.3, an edge-on orbit for the secondary is excluded from the lack of transits for reasonable assumptions about its radius.

The minimum mass and mass ratio of the tertiary are much more poorly constrained due to the incomplete phase coverage of the orbit. We find median and 68% confidence intervals of

$$M_{3,\min} = 426^{+261}_{-98}\, M_{\rm Jup} = 0.407^{+0.249}_{-0.093}\, M_\odot,$$
$$q_3 = 0.334^{+0.205}_{-0.0761}. \quad (5)$$

The uncertainties in these quantities contain significant contributions from both the uncertainty in the host star mass and the tertiary mass function.

5. IMAGING

Lucky Imaging (Fried 1978) was performed in 2010 October and 2011 October using FastCam (Oscoz et al. 2008) on the 1.5 m TCS telescope at Observatorio del Teide in Spain to search for companions at large separations from the primary star. Lucky Imaging consists of taking observations at very high cadence to achieve nearly diffraction-limited images from a subsample of the total. During the 2011 October observations, the CCD gain was adjusted, and therefore that night's data are analyzed as two different image sets. For the 2010 October data, a total of 140,000 frames comprised of 50 ms integrations were obtained in the *I*-band spanning $21'' \times 21''$ on sky. For the 2011 October observations, a total of 31,000 frames comprised of 50 ms integrations were obtained in the low-gain setting, and 100,000 frames comprised of 40 ms integrations were obtained in the higher-gain setting. Image selection is applied using a variety of selection thresholds (best *X*%) based on the brightest pixel (BP) method, making sure that non-speckle features are avoided.

The BPs of each frame are then sorted from brightest to faintest, and the best *X*% are then shifted and added to generate a final image, where $X = \{15, 85\}$. The effective Strehl ratios for $X = 85\%$ are $\{0.036, 0.037, 0.043\}$ for the three image sets, respectively. Figure 6 shows composite images for $X = 15\%$ and 85% of the frames for each set of observations. The intensities are detector counts on a linear scale after being stacked and normalized by the number of images used in the stacking. The artifact in the 2010 October frames is a result of imperfect telescope tracking. No companion is detected at the 3σ level, where σ is defined using the procedure in Femenía et al. (2011) based on the rms of the counts within concentric annuli centered on TYC 2930 and using 8 pixel boxes.

In addition to the Lucky Imaging, we conducted AO imaging to search for any wide stellar companions to TYC 2930. The Keck AO images were obtained with NIRC2 (PI: K. Matthews) on UT 2011 August 30. The observations were conducted in the K' band using the narrow camera setting, resulting in a plate scale of 9.963 mas pixel^{-1} (Ghez et al. 2008). The total integration time was 65 s using a three-point dither pattern. Images were processed using standard pixel cleaning,

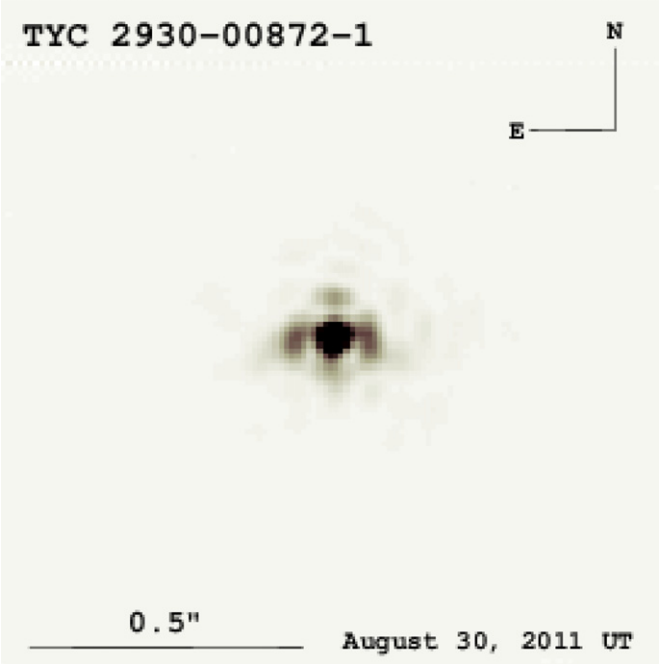

Figure 7. Keck AO image of TYC 2930. No stellar companions are detected at the 3σ level beyond $\sim$200 mas $\simeq$ 30 AU, corresponding to a brightness limit of $\Delta m \sim 6$.

(A color version of this figure is available in the online journal.)

flat-fielding, and stacking procedures. Figure 7 shows the processed Keck AO image; no evidence for wide stellar companions can be seen. Detectability curves (3σ) are calculated as a function of separation from TYC 2930 for both the Lucky Imaging and AO data. Contrast ratios are converted into mass sensitivities using the Baraffe et al. (2003) models for the Keck band and Girardi et al. (2002) models for the Lucky Imaging band. As can be seen in Figure 8, we can exclude stellar companions at projected separations greater than $\sim$50 AU. While the Keck constraints are superior compared to the Lucky Imaging constraints, they also rely on a very expensive resource (namely, the Keck telescope). Since Lucky Imaging can be conducted on much smaller and more readily available telescopes, it is a good resource to use in the search for wide companions in the absence of 10 m telescope access.

6. ANALYSIS OF THE RELATIVE PHOTOMETRY

6.1. Summary of Data Sets

The WASP photometric data set for TYC 2930 consists of 3975 points spanning roughly two years from HJD$'$ = 3831 to 4571. The full, detrended WASP data set has a relatively high weighted rms of 2.9% and exhibits evidence for systematics. The distribution of residuals from the weighted mean is asymmetric and highly non-Gaussian, showing long tails containing a much larger number of $>3\sigma$ outliers than would be expected for a normally distributed population.

We clean the WASP data by adding in quadrature to the photon noise a systematic uncertainty ($\sigma_{\rm sys}$) that results in a distribution of residuals closest to the Gaussian expectation. We reject the largest, error-normalized outlier from the mean flux value and scale the uncertainties by a factor r to force χ^2/dof = 1, iterating until no more outliers $> 4\sigma$ remain. Although 4σ is a slightly larger deviation than we would expect based on the final number of points, we adopt this conservative threshold to avoid removing a potential transit signal. We find $r = 0.39$ and $\sigma_{\rm sys} = 0.0053$, retaining 3731 data points with an rms of 0.71% and χ^2/dof = 1 (by design).

The Allegheny photometric data set consists of 1280 points spanning roughly 44 nights from HJD$'$ = 5596 to 5640. The weighted rms of the raw light curve is 0.48%; this is a factor of $\sim$3 times smaller than the average fractional photometric uncertainties, indicating that these errors have been overestimated. Although there is no clear evidence for systematic errors in this data set, we repeat the identical procedure as with the WASP data for consistency. We find $r = 0.38$ and $\sigma_{\rm sys} = 0.0011$, with a final rms of 0.42% from 1274 data points.

The KELT data set consists of 2781 data points spanning roughly 3 years from HJD$'$ = 4107 to 5213. The weighted rms of the raw light curve is 0.62%, and the mean uncertainty is 0.55%, indicating that these are reasonably well estimated. Nevertheless, for consistency we clean the data in the same way as the other two data sets, finding no outliers $>4\sigma$, $r = 1.09$, and $\sigma_{\rm sys} = 0.0021$, with a final rms of 0.62%.

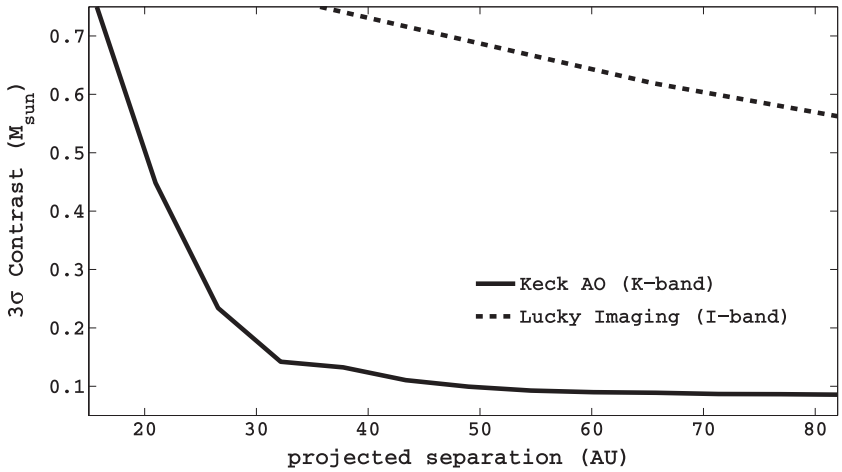

Figure 8. Detectability (contrast curve) for the Lucky Imaging and Keck AO images of TYC 2930. Contrast levels are converted to masses based on Baraffe et al. (2003) models for the Keck band and Girardi et al. (2002) isochrones for the Lucky Imaging band. A separation of 50 AU is $\sim$350 mas at TYC 2930's *Hipparcos*-based distance of $\sim$140 pc.

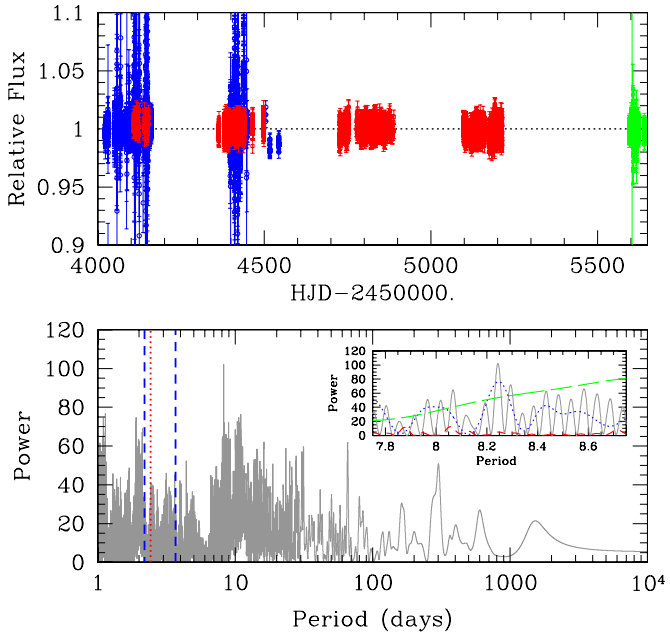

Figure 9. Top panel: cleaned relative photometry of TYC 2930 from WASP (blue), KELT (red), and Allegheny (green). Bottom panel: Lomb–Scargle periodogram of the combined photometric data. While a large number of strong peaks are visible, we do not regard these as significant. There is no strong peak at the period of the secondary (vertical red dotted line) or within the estimated 2σ period range of the primary's rotational period (vertical blue dotted lines). The inset shows detail of the most significant peak in the combined periodogram (gray), as well as the periodograms for just the WASP (blue dotted), KELT (red short dashed), and Allegheny (green long dashed) data sets. The peak in the combined data set arises almost exclusively from the WASP data and is not confirmed by the KELT data.

(A color version of this figure is available in the online journal.)

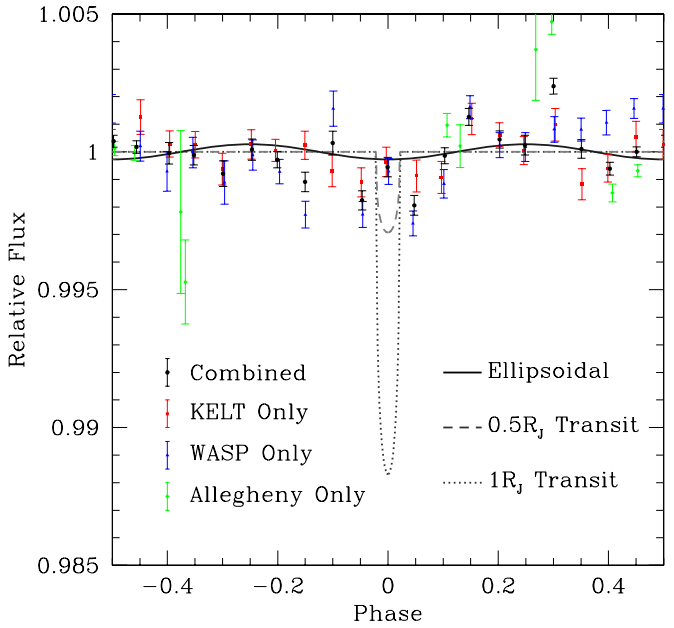

Figure 10. Relative photometry folded at the period of secondary and binned 0.05 in phase. Phase zero corresponds to the expected time of conjunction (and so of transits for the appropriate inclinations). Black points are the combined data, blue are WASP, red are KELT, and green are Allegheny. The gray curves show the expected transit signatures for a companion with radius of 0.5 $R_{\rm Jup}$ (dashed) and 1 $R_{\rm Jup}$ (dotted), assuming an edge-on inclination and the median estimated values of the primary mass and radius. The solid curve shows the expected signature of ellipsoidal variability assuming an edge-on companion.

(A color version of this figure is available in the online journal.)

Finally, we combine all the relative photometry after normalizing each individual data set by its mean weighted flux. The top panel of Figure 9 shows the combined data set, which consists of 7786 data points spanning roughly 4.4 years from HJD′ = 4022 to 5640 and has a weighted rms of 0.58%. The resulting light curve is constant to within the uncertainties over the entire time span. Within the KELT data set, which spans ∼3 years, we find no strong evidence for long-term intrinsic variability at a level $\gtrsim$0.6%.

6.2. Search for Periodic Variability

We ran a Lomb–Scargle periodogram on the full data set, testing periods between 1 and 10^4 days. The resulting periodogram, shown in the bottom panel of Figure 9, displays a large number of formally significant peaks. The inferred amplitudes are all $\lesssim$0.1%; similar to the level of systematic errors inferred when cleaning the light curves. A comparison of periodograms performed on the individual data sets demonstrates that the strongest peaks arise from only one data set and are not corroborated by the other data sets. The most significant peak in the combined data set has a period of 8.24 days, with a power of ∼100 and an amplitude of ∼0.13%. However, as shown in the inset, the signal comes almost entirely from the WASP data set (blue). In general, the KELT data set (red) shows significantly reduced power on all periods $\lesssim$100 days; the rms of the periodogram in this range is only ∼4, as compared ∼14 for the combined data set. Although the different results inferred for different data sets could in principle arise from real variability that is not strictly periodic or persistent, it is more likely that there exist systematics in the data sets in the form of residual correlations on a range of timescales.

Restricting attention to periods within 10σ of that inferred for the companion ($P = 2.430420 \pm 0.000006$ days), the maximum power is ∼20 with an amplitude of only ∼0.06%, a factor of ∼10 times smaller than the rms of the light curve. Considering an expanded range of periods within 2σ of the period of the primary as inferred from the $R'_{\rm HK}$ index ($P = 2.93 \pm 0.37$ days, see Section 7), the maximum power is ∼46 with an amplitude of ∼0.09%. We do not regard these maxima as significant, and conclude that the star does not exhibit periodic variability at either the expected rotation period of the star or the period of the inner companion at a level $\gtrsim$ 0.1%.

Figure 10 shows the combined light curve, folded at the median period and time of conjunction of the companion, ($P = 2.430420 \pm 0.000006$ days and $T_C = 2454842.2640$), and binned in phase using bins of 0.05. The weighted rms of the binned light curve is ∼0.087%. Although the variations are larger than expected from a constant light curve based on the uncertainties (χ^2/dof ∼ 9), we again suggest that these are due to systematic errors in the relative photometry. In particular, the folded, binned KELT light curve (red) shows a somewhat lower rms of ∼0.068% with a χ^2/dof = 1.8 and is more consistent with a constant flux. We conclude that there is no strong evidence for variability of TYC 2930 on any timescale we probe. We can robustly constrain the amplitude of any persistent, periodic variability to be less than $\lesssim$ 0.1%, and we can constrain the amplitude of photometric variability at the period of the companion to $\lesssim$0.07%.

Given the estimated stellar mass, the companion period, and the minimum mass, the amplitude of ellipsoidal variability is

expected to be

$$\delta_{\rm ellip} \sim 0.03\%(m_2 \sin I/67 M_{\rm Jup}) \times (M_1/1.2\ M_\odot)(P/2.43\,{\rm d})^{-2} \sin I \quad (6)$$

with a period of $P/2$ (Pfahl et al. 2008). This expected signal is compared to the binned data in Figure 10, demonstrating that it is just below the level of detectability. Since smaller inclinations lead to lower amplitudes, we are unable to constrain the inclination using ellipsoidal viability.

6.3. Excluding Transits of the Secondary

The probability that low-mass companion transits can be determined given the orbital parameters from the RV solution (Kane & von Braun 2008). Assuming a uniform distribution in $\cos i$, the a priori transit probability for the secondary is relatively high, ~13%. However, the light curve folded on the ephemeris of the inner companion shows no evidence for a transit at the expected time of conjunction, with an upper limit to the depth of any putative transit of $\lesssim$0.2%. In contrast, the central transit of a Jupiter-sized companion would be expected to have a depth of $\delta \sim (r/R_1)^2 \sim 0.9\%$ and a duration of ~0.042 in phase. We conclude that our observations rule out such a transiting companion with high confidence.

We perform a quantitative search for transit signals using a method similar to that described in Fleming et al. (2010). We use the distributions of the secondary period P, semiamplitude K, and time of conjunction T_c from the MCMC RV analysis, setting the eccentricity of the secondary to zero for simplicity. For each link in the MCMC chain, we draw a value of $T_{\rm eff}$, $\log g$, and [Fe/H] for the primary from Gaussian distributions, with means and dispersions given in Table 3, and determine the primary's mass M_1 and radius R_1 using the Torres et al. (2010) relation on these values.

We then draw a value of $\cos i$ from a uniform distribution,[24] and use the resulting values of P, K, M_1, R_1, and i to determine the secondary mass m_p, semimajor axis a, and impact parameter of the secondary orbit $b \equiv a \cos i R_1^{-1}$. Finally, adopting a radius for the companion, r, we determine if the companion transits, and if so we determine the properties of the light curve using the routines of Mandel & Agol (2002). We assume quadratic limb darkening and adopt coefficients appropriate for the R band from Claret & Hauschildt (2003), assuming solar metallicity and the values of $T_{\rm eff}$ and $\log g$ listed in Table 3. For reference, Figure 10 shows the predicted transit signatures for the median values of the physical parameters and $r = 0.5\ R_{\rm Jup}$ and $1\ R_{\rm Jup}$. We fit the predicted transit light curve to the combined photometric data, and then compute the $\Delta\chi^2$ between the constant flux fit and the predicted transit model.

Our best fit has a $\Delta\chi^2 = -19.8$, which we do not consider significant. We find similar or larger improvements in χ^2 when we consider arbitrary phases for the transit and when we consider "anti-transits" (signals with the same shape as transits but corresponding to positive deviations; see Burke et al. 2006). As before, these formally significant signals likely arise from systematics in the photometric data. We conclude there is no evidence for a transit signal in the combined data.

Given that we do not detect a transit signature, we can also use this procedure to determine the confidence with which we can rule out transits of a companion with a given radius. This is just given by the fraction of the steps in the Markov Chain for which the companion transits and produces a transit signature with a $\Delta\chi^2$ relative to the fixed constant flux greater than some threshold. We consider thresholds of $\Delta\chi^2 = 9$, 16, and 25. The resulting cumulative probability distributions for a range of companion radii are shown in Figure 11. Given the systematics in the data, we consider thresholds of $\Delta\chi^2 \gtrsim 25$ to be robust, and thus conclude that transiting companions with $r \gtrsim 0.75\ R_{\rm Jup}$ are likely ruled out at the ~95% confidence level. The models of Baraffe et al. (2003) predict radii of $\gtrsim$0.8 $R_{\rm Jup}$ for BDs of $m_p \sim 60\ M_{\rm Jup}$ and ages of $\lesssim$5 Gyr. Given the upper limit of the age of the primary of ~2 Gyr, we can therefore essentially rule out non-grazing transits of the companion.

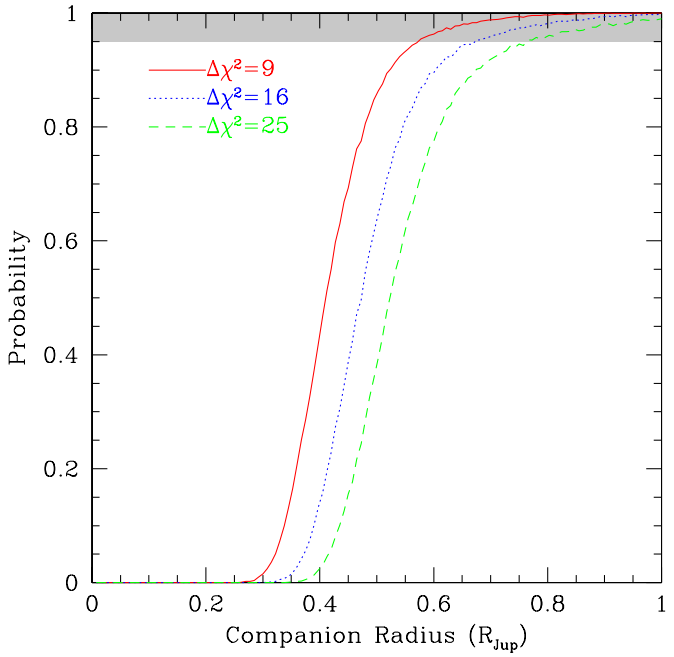

Figure 11. Probability that transits of a companion are excluded at levels of $\Delta\chi^2 = 9, 16, 25$ based on the analysis of the combined WASP, KELT, and Allegheny photometric data sets, as a function of the radius of the companion. Transits of companions with radius $r \geqslant 0.7\ R_{\rm Jup}$ can be excluded at the 95% confidence level.

(A color version of this figure is available in the online journal.)

7. CONSTRAINTS ON SYSTEM GEOMETRY AND TIDAL ANALYSIS

The rotational period of a star can be estimated from an empirical relationship between the Rossby number and $\log R'_{\rm HK}$ (Noyes et al. 1984). The Rossby number $R_0 = P\tau_c^{-1}$, where P is the rotation period of the star and τ_c is the convective turnover time. In this work, we use the relationship as quantified by Mamajek & Hillenbrand (2008). We estimate the convective turnover time based on the relationship between R_0 and $(B-V)$ from Noyes et al. (1984). We find an expected rotational period based on the measured $\log R'_{\rm HK}$ of $P = 2.93 \pm 0.37$ days. The uncertainty in the period includes the uncertainty in the Mamajek & Hillenbrand (2008) relationship, as well as an adopted uncertainty in $R'_{\rm HK}$ of 0.2×10^{-5} based on the observed variability of the most active stars in the Lovis et al. (2011) sample. The latter uncertainty accounts for the fact that the Mamajek & Hillenbrand (2008) relation applies to a time-averaged $R'_{\rm HK}$, while we have a single epoch measurement. The modest upper limit on the rotation rate of $v \sin I < 6\,{\rm km\,s^{-1}}$,

[24] Formally, this assumes a prior on the companion mass m_p that is uniform in $\log m_p$.

the fact that the estimated rotation rate from the Mamajek & Hillenbrand (2008) relation is close to the orbital period of the inner companion, and the expected equatorial rotation velocity of $22.68 \pm 3.12\,\mathrm{km\,s^{-1}}$ if the primary was rotating at the inner companion's orbital period and had a stellar spin axis oriented edge-on, all suggest that the primary's spin axis is inclined relative to our line of sight, in which case the inclination is constrained to be $I = 15.0^{+7.3}_{-6.2}$ deg.

We can use the reasonably strong upper limit on TYC 2930's photometric variability to place additional limits on the inclination of the star and its companion. The lack of photometric variability is somewhat surprising, given the spectroscopic indications that the star is relatively active. An estimate of the expected photometric variability can be obtained using the relationship in Hartman et al. (2009) between R_0 and photometric amplitude. Based on the estimated R_0 from the Mamajek & Hillenbrand (2008) R_0–log $R'_{\rm HK}$ relationship, we would expect a photometric amplitude of ∼0.8%. Figure 17 in Hartman et al. (2009) indicates that there exists substantial scatter about this relation, which is likely partially suppressed for values of $R_0 \gtrsim 0.4$ due to incompleteness. Extrapolating the observed scatter at lower values of R_0 (which are less affected by incompleteness), we expect a photometric amplitude in the range of ∼0.2%–2%. Thus, the fact that the observed amplitude is at least a factor of ∼3 times lower ($\lesssim$0.07%) suggests that this star is either surprisingly photometrically quiet given its spectroscopic activity indicators, or is it being viewed nearly pole-on.

The expectation of a synchronous rotation rate for the primary is reinforced by consideration of the tidal evolution of the primary and secondary. To analyze this effect, we employed the "constant-phase-lag" (CPL) tidal model in which the location of the tidal bulge on the two bodies lies at a constant angle from the line connecting the centers of the two bodies. Frictional forces inside the two objects prevent perfect alignment, which leads to energy dissipation and transfer of angular momentum. Hence, the system will evolve with time (see, e.g., Goldreich & Soter 1966; Ferraz-Mello et al. 2008). Two outcomes are possible: arrival at the "double synchronous" state, in which the obliquities are normal to the orbital plane, and the two spin frequencies equal the orbital frequency, or the two bodies merge (Counselman 1973). Here, we use the CPL model presented in Ferraz-Mello et al. (2008), with the numerical methods described in Barnes et al. (2012, Appendix D).

In the CPL model, the tidal effects scale with the "tidal quality factor" Q_*. This parameter is poorly constrained in stars and BDs with values ranging from 10^5 to 10^9 (e.g., Lin et al. 1996; Matsumura et al. 2008); therefore we explore the timescale to reach the double synchronous state in this range. The masses and radii of the two objects are also important, and although we have constraints on the two masses and the primary's radius, the secondary's radius is unknown. We adopt a radius of 1 Jupiter mass, in line with theoretical models (Baraffe et al. 2003).

For compact binaries, tidal evolution during the pre-main-sequence phase is also important (Zahn & Bouchet 1989; Khaliullin & Khaliullina 2011; Gómez Maqueo Chew et al. 2012), since the radii are larger. As tidal effects scale with radius to the fifth power, the results can be dramatic. Most stellar binaries with periods less than eight days are on circular orbits and probably near the double synchronous state (Zahn & Bouchet 1989), suggesting the TYC 2930 system could also have reached this state early in its history. On the other hand, the inner companion could have arrived at its orbit after the radial contraction phase, perhaps via a gravitational scattering event

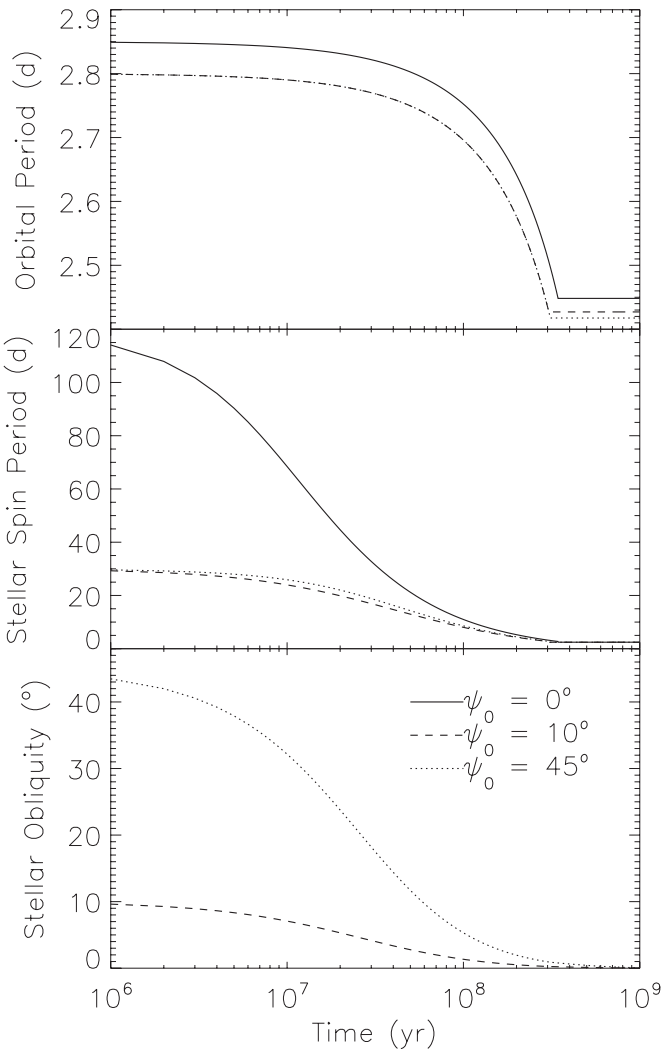

Figure 12. Tidal evolution of the TYC 2930 system. Curves represent assumed initial stellar obliquity values of $\psi_0 = 0°$ (solid), 10° (dashed), and 45° (dotted). Top: evolution of the orbital period. Middle: evolution of the stellar spin period. Bottom: evolution of the stellar obliquity.

(Heggie 1975), or due to Kozai–Lidov interaction followed by tidal circularization (Fabrycky & Tremaine 2007). Therefore, in order to be as conservative as possible, we will ignore any evolution during the pre-main sequence. We therefore consider our timescales to reach double synchronization to be upper limits.

In Figure 12, the evolutions of the orbital period, stellar spin period, and stellar obliquity, ψ, are shown for three different cases of initial obliquities: $\psi_0 = 0°$ (solid curves), $\psi_0 = 10°$ (dashed curves), and $\psi_0 = 45°$ (dotted curves). For each case, the initial spin period is 30 days, the secondary has a mass of 100 $M_{\rm Jup}$, the initial orbital period is 2.8 days, and the stellar tidal quality factor Q_* is 10^7. In each model, the orbital and spin periods reach ∼2.43 days and become locked after ∼300 Myr. The obliquity can evolve slightly longer, but with negligible effect on the spins and orbit. Double synchronization requires $\psi = 0°$ and hence the timescale to reach that state is larger when the initial ψ is nonzero.

The initial spin period of the star is unknown, and therefore we tested values larger than 30 days. For the extreme case of a 120 days period and $\psi_0 = 45°$, the time to reach double synchronization is about three times longer than the cases shown in

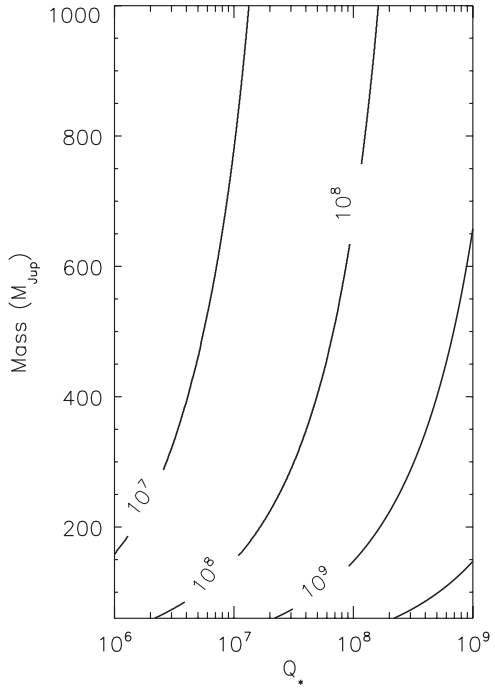

Figure 13. Time (years) for TYC 2930 to reach double synchronization. The star initially has no obliquity and a rotation period of 30 days. The companion is tidally locked. No non-tidal effects, such as an early epoch of radial contraction, are included.

Figure 12. For this initial configuration, an initial orbital period of 2.85 days produces a better match to the observed system.

We expanded our analysis to a range of M_2 and Q_* to determine which values predict the double synchronized state on a timescale less than or equal to the system age of <2 Gyr. Initially, we set the primary spin period to 30 days and ψ_0 to 0° (as shown in Figure 12, different choices do not affect our results), the secondary's spin period was always tide-locked, and the initial orbit was circular with a period of 2.8 days. We then integrated forward a suite of configurations in the ranges $60 \leqslant M_2 \leqslant 1000\ M_{\rm Jup}$ and $10^6 \leqslant Q_* \leqslant 10^9$ and calculated the timescale to reach double synchronization. We considered this state achieved when the stellar spin period was within 10% of the orbital period. Figure 13 shows the timescale for double synchronization as a function of inner companion mass and Q_*. For the minimum mass, double synchronization will occur within the nominal 2 Gyr lifetime if $Q_* \lesssim 3 \times 10^7$, while at $M_2 = 300\ M_{\rm Jup}$, Q_* must be $<4 \times 10^8$. Our tidal analysis strongly favors the double synchronous state.

8. A POSTERIORI DISTRIBUTIONS OF THE TRUE MASS

The a posteriori distribution of the true mass of the companions given our measurements depends on our prior distribution for the mass of the companion, or, roughly equivalently, our prior on the mass ratio. As a rough illustration, if we assume a prior that is uniform in the logarithm of the true mass of the companion, then the distribution of $\cos i$ will be uniform. Therefore, the median $\cos i \simeq 0.5$, and thus the median $\sin i \simeq 0.866$. Thus, we have

$$0.75^{3/2}\, M_J^3 - \mathcal{M}_j (M_1 + M_j)^2 = 0, \tag{7}$$

where $j = 2, 3$ refers to the secondary and tertiary, respectively. For the secondary, $\mathcal{M}_2 = 1.6711 \times 10^{-4}$ and $M_1 = 1.21\ M_\odot$; the solution is $M_2 \simeq 0.0752\ M_\odot$ or $\sim$78.75 $M_{\rm Jup}$. This result is roughly $M_{2,\rm min}/\sqrt{0.75}$, but not exactly. For the tertiary, the median mass is $M_3 \sim 0.48\ M_\odot$.

More generally, for other priors, $\cos i$ is not uniformly distributed. We adopt priors of the form:

$$\frac{dN}{dq} \propto q^\alpha, \tag{8}$$

where q is the mass ratio between the companion and the primary, and $\alpha = -1$ for the uniform logarithmic prior discussed above. To include this prior, we draw a value of $\cos i$ from a uniform distribution for each link in the MCMC chain, but then weight the resulting values of the derived parameters for that link (i.e., the companion mass m) by $q^{\alpha+1}$. In addition, based on the analysis of the relative photometry in Section 6.3, we exclude transiting configurations of the secondary such that $b \equiv a \cos i_2 R_1^{-1} < 1$.

For $q > 0$, the a posteriori distribution does not converge, i.e., there is finite probability at infinitely large true masses. However, we can rule out nearly equal mass ratio main-sequence companions by the lack of any evidence of additional light beyond that from the primary, in particular from the lack of a second set of spectral lines and from the shape of the SED. As we describe below, both of these constraints place an upper limit on the mass of any main-sequence companion to $\lesssim 1\ M_\odot$. We adopt this limit by giving zero weight to inclinations of the secondary and tertiary such that $M_{2,3} \geqslant 1\ M_\odot$. In doing so, we implicitly assume that neither of these companions are stellar remnants.

The optical/near-infrared colors of the primary are well fit by a model for the SED appropriate to a star with the effective temperature and surface gravity we measure from the spectrum (see Figure 1). A sufficiently massive main-sequence companion would contribute near-IR flux in excess of that predicted from the primary. We can therefore use the lack of excess flux to constrain the mass of the secondary (and tertiary). We generate a set of two-component SEDs using Baraffe et al. (1998, 2003) models, adopting stellar parameters for the primary from Table 3 and models corresponding to tertiary masses from 0.2 to 1.2 $M_\odot$. We then fit the observed fluxes with these two-component SEDs, allowing distance and line-of-sight extinction to be free parameters. For each tertiary mass, we calculate a $\chi^2 = \chi^2_{\rm SED} + \chi^2_{\rm dist}$, where $\chi^2_{\rm SED}$ is based on the observed fluxes and $\chi^2_{\rm dist}$ is based on the *Hipparcos* parallax. We compute a $\Delta\chi^2 = \chi^2_{\rm 2comp} - \chi^2_{\rm 1comp}$, where $\chi^2_{\rm 1comp}$ is the χ^2 for the single-component (i.e., primary-only) SED fit. We then use these $\Delta\chi^2$ to determine an upper limit of the tertiary mass by rejecting those tertiary masses that yield $\Delta\chi^2 > 0$, finding $M_3 \lesssim 1\ M_\odot$. A similar mass constraint is derived by visual inspection of the cross-correlation functions from the spectroscopic observations. Assuming none of the components are evolved, mass ratios of ~ 0.8 can be excluded at the maximum RV separation between the primary and tertiary ($\sim$5 km s^{-1}) due to a lack of asymmetry in the correlation peaks, once again constraining $M_3 \lesssim 1\ M_\odot$.

Finally, as discussed in Section 7, the rotational period of the primary P_* as estimated from the $R'_{\rm HK}$ index is within 1.5σ of the period of the secondary, suggesting that the primary spin may be synchronized to the companion orbit. This hypothesis is corroborated by our tidal analysis, which suggests that for reasonable values of the stellar Q_* this system should reach a double-synchronized state in which the obliquities are aligned with the orbit within 100 Myr, which is considerably less than our estimate of the age of the system. Therefore, adopting

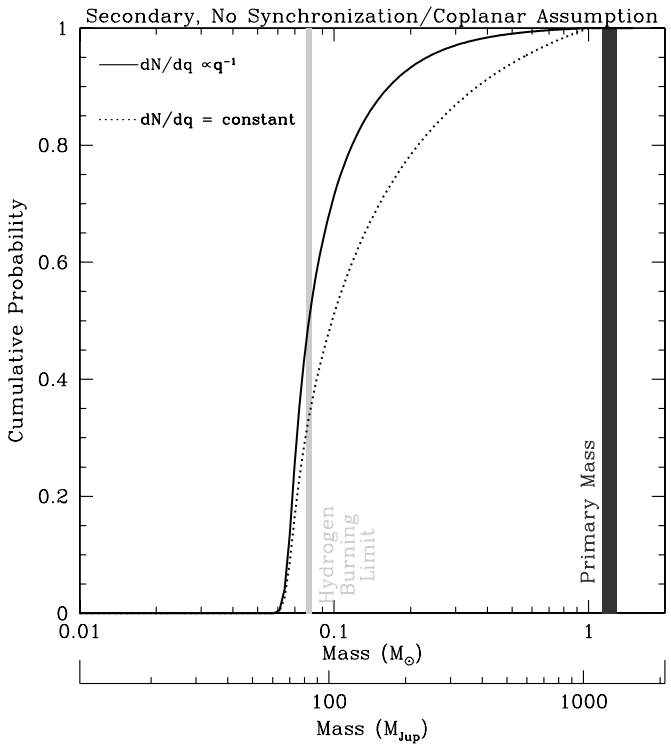

Figure 14. Cumulative a posteriori probability of the true mass of the secondary, for two different priors on the mass ratio q: $dN/dq \propto q^{-1}$ (uniform in $\log q$) and dN/dq = constant (uniform in q). Companion masses $\geqslant 1\,M_{\odot}$ and transiting configurations are excluded.

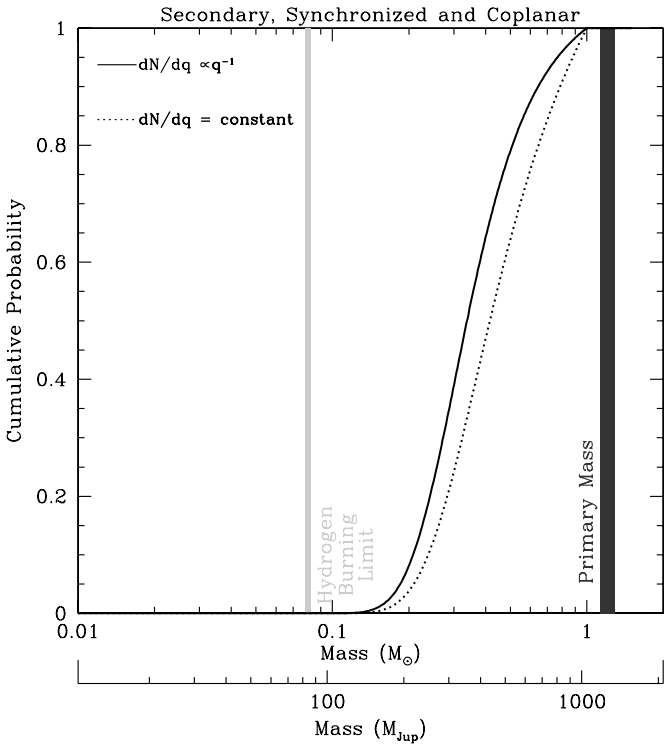

Figure 15. Cumulative a posteriori probability of the true mass of the secondary under the same set of assumptions as Figure 14, but assuming that the primary and secondary are synchronized and the stellar obliquity has been damped to zero, and thus the inclination of the star I as determined from the observed velocity broadening $v_* \sin I$ and stellar rotation period P_* is equal to the inclination of the orbit of the secondary i.

Table 6
A Priori Secondary Mass

α[a]	Key[b]	Median M_2, 68%	Median i_2, 68%	Transit Prob.
−1	1	$0.080^{+0.048}_{-0.012}$	$56.0^{+18.7}_{-24.8}$	0.133
0	1	$0.098^{+0.160}_{-0.028}$	$42.4^{+27.2}_{-26.3}$	0.086
−1	2	$0.338^{+0.216}_{-0.110}$	$12.6^{+5.2}_{-4.2}$	<0.001
0	2	$0.416^{+0.280}_{-0.150}$	$10.6^{+5.0}_{-3.6}$	<0.001

Notes.
[a] Prior of the form: $N/dq \propto q^{\alpha}$.
[b] 1 = flux ratio and transit constraint. 2 = flux ratio, trasit, and synchronization/coplanarity.

this synchronized/coplanar assumption, we have $I = i_2$ and $P_* = P_2$. We can use these assumptions, combined with the constraints on $v \sin I = 3.8^{+1.9}_{-2.8}\,\mathrm{km\,s^{-1}}$ from the spectroscopic analysis of the primary, to constrain i_2 and thus the true mass of the companion. For each link in the MCMC chain, we use the value of i_2, R_1, and secondary period P_2 to estimate $v \sin I = v \sin i_2 = (2\pi R_1/P_2) \sin i_2$. We then multiply the weight of that chain by the additional factor $\exp[-0.5(v \sin I - 3.8\,\mathrm{km\,s^{-1}})^2/\sigma^2_{v \sin I}]$ where $\sigma_{v \sin I} = 2.8\,\mathrm{km\,s^{-1}}$ for $v \sin I < 3.8\,\mathrm{km\,s^{-1}}$ and $\sigma_{v \sin I} = 1.9\,\mathrm{km\,s^{-1}}$ for $v \sin I > 3.8\,\mathrm{km\,s^{-1}}$.

Figures 14–16 show the resulting cumulative a posteriori distributions of the true masses of the companions under several sets of assumptions. These figures illustrate the effect of adopting various priors and constraints on our inferences about the nature of these companions. Tables 6 and 7 list the median and 68% confidence intervals on the true masses of the companions. We will discuss each model in turn.

Figure 14 shows the results for the secondary, for $\alpha = -1$ (uniform logarithmic prior on q) and $\alpha = 0$ (uniform linear prior

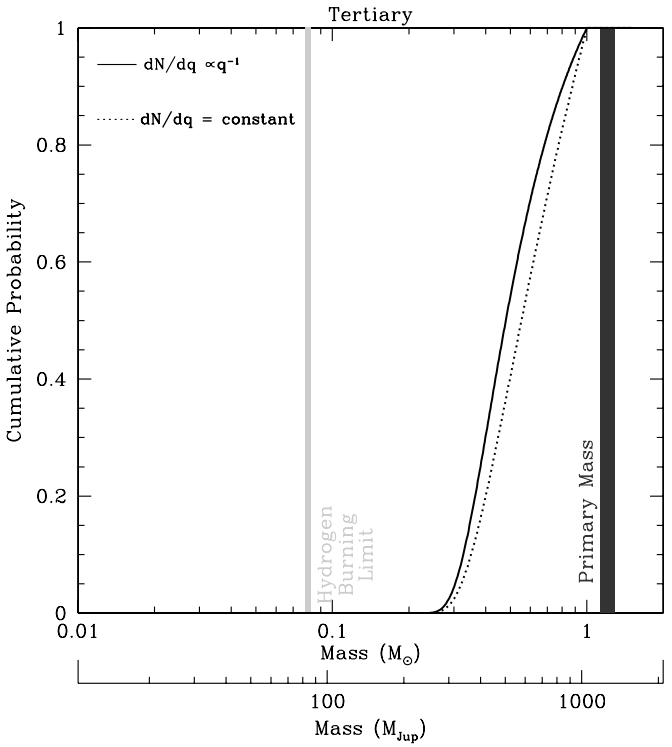

Figure 16. Cumulative a posteriori probability of the true mass of the tertiary under the same set of assumptions as Figure 14, except that transiting configurations are not excluded.

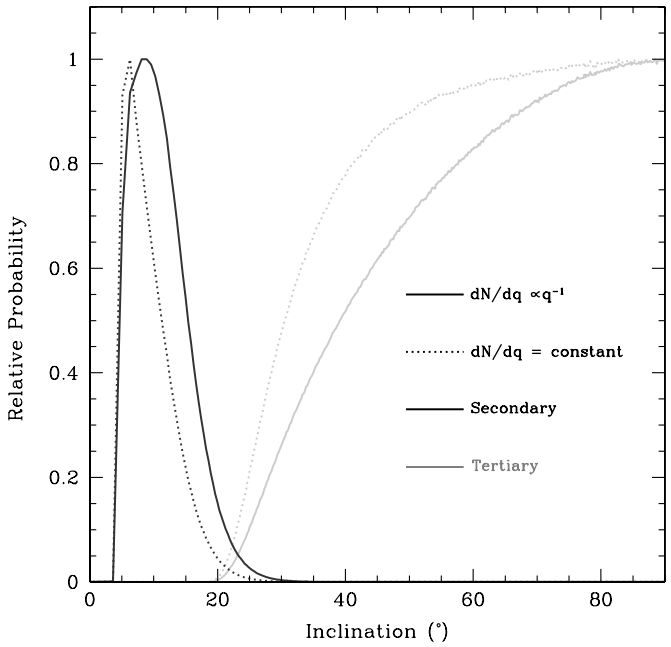

Figure 17. A posteriori probability densities for the inclinations of the tertiary and secondary. These curves have been arbitrarily normalized by their peak probability density. The black lines show the probabilities for the secondary assuming the tidal synchronization/coplanarity, for two different priors on the mass ratio q, $dN/dq \propto q^{-1}$ (uniform in $\log q$, solid), and $dN/dq =$ constant (uniform in q, dotted). The gray lines show the probabilities for the tertiary, for the same priors on the mass ratio. In all cases, we exclude companion masses $\gtrsim 1\ M_\odot$.

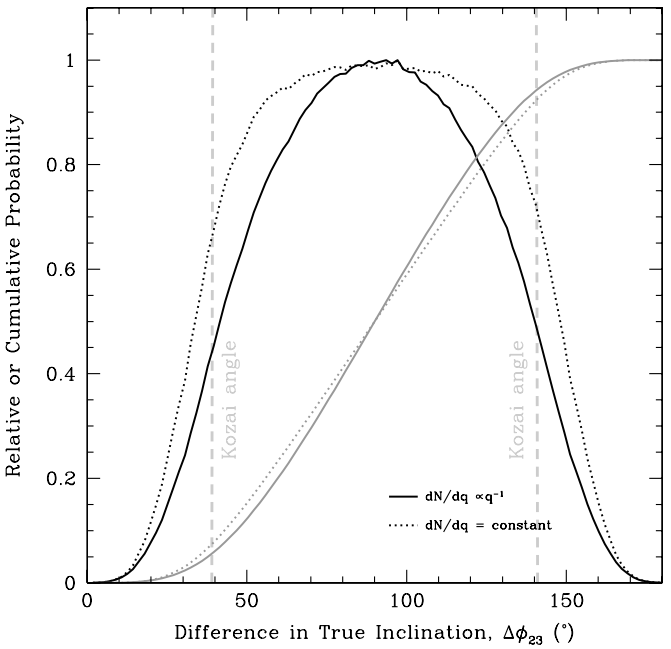

Figure 18. A posteriori probability density (black lines) and cumulative probability (gray lines) for the true relative inclination of the secondary and tertiary $\Delta\phi_{23}$. The probability densities have been arbitrarily normalized by their peak probability density. The solid lines show the probabilities assuming a prior on the mass ratio q of $dN/dq \propto q^{-1}$ (uniform in $\log q$), where as the dotted lines show $dN/dq =$ constant (uniform in q). In both cases, tidal synchronization/coplanarity for the secondary has been assumed, and companion masses $\gtrsim 1\ M_\odot$ have been excluded. The curves are symmetric about $\Delta\phi = 90°$ because translating the inclinations of the secondary and tertiary by π results in the same observables.

Table 7
A Priori Tertiary Mass Including Flux Ratio Constraint

α	Median M_3, 68%	Median i_3, 68%	Transit Prob.
−1	$0.480^{+0.245}_{-0.131}$	$65.4^{+17.1}_{-21.2}$	0.001
0	$0.553^{+0.261}_{-0.173}$	$61.5^{+19.5}_{-25.4}$	0.001

on q), assuming the constraint from the lack of transits and the upper limit on the mass of $M_\odot$ from the lack and evidence of light from the companion. The constraint that $M_2 \leqslant 1\ M_\odot$ makes little difference for $\alpha = -1$, because the companion is unlikely to be sufficiently massive to contribute a significant amount of flux. For $\alpha = 0$, the prior on the companion mass is more heavily weighted to larger masses, and as a result this constraint does affect the high-mass tail of the probability distribution; nevertheless, the inferred median masses in the two cases are similar. Under these assumptions, we would conclude that the secondary is most likely a low-mass stellar or BD companion seen at a moderate inclination of ∼40°–60°, with a median mass just above the hydrogen-burning limit $M_2 \sim 0.08$–$0.1\ M_\odot$.

Assuming synchronization and coplanarity changes the conclusion about the nature of the secondary dramatically, given that the spectroscopically measured $v \sin I$ suggests a relatively low inclination for the primary of ∼15°. Figure 15 shows the inferred cumulative distribution for the secondary, for $\alpha = 0$ and $\alpha = -1$ and assuming the upper limit on the mass. The results for the two priors are broadly similar: under the synchronization assumption the secondary is most likely a mid M dwarf with $M_2 \sim 0.3$–$0.4\ M_\odot$ with a nearly pole-on orbit with $i_2 \sim 10°$–$13°$.

Figure 16 shows the cumulative distributions of the true mass of the tertiary. The mass of the tertiary is limited from below to be $\gtrsim 0.2\ M_\odot$ by the measured mass function, and from above to be $\lesssim 1\ M_\odot$ by the lack of light from the companion. The choice of prior on q has a relatively weak affect on the distribution of masses within this range. The tertiary is most likely to be an early M dwarf with a mass of ∼0.5–0.6 $M_\odot$ with a moderate inclination of $i_3 \sim 60°$–$70°$.

Adopting the synchronization/coplanarity assumption, we infer that the secondary is seen nearly pole-on, whereas from the lack of evidence for additional light from a companion, we infer that the tertiary cannot be very massive and thus cannot have a low inclination. Figure 17 shows a posteriori probability densities for the inclinations of the tertiary and secondary under these assumptions. The 95% confidence level (c.l.) upper limit on the secondary inclination including the synchronization/coplanarity constraint and flux constraint is 23.°6 ($\alpha = -1$) and 21.°2 ($\alpha = 0$). On the other hand, the 95% c.l. lower limit on tertiary inclination including the flux constraint is 30.°1 for $\alpha = -1$ and 28.°1 for $\alpha = 0$. The difference in the orbital inclinations with respect to the sky plane $|i_1 - i_2|$ is a lower limit to the true mutual inclination, and thus under these assumptions the orbits are misaligned at the $> 95\%$ c.l.

The true mutual inclination $\Delta\phi_{23}$ of the orbits is related to the inclinations referenced to the sky plane by

$$\cos\Delta\phi_{23} = \cos i_2 \cos i_3 + \sin i_2 \sin i_3 \cos(\Delta\Omega_{23}), \qquad (9)$$

where $\Delta\Omega_{23} \equiv \Omega_2 - \Omega_3$ and Ω_j is the longitude of the ascending node for companion j. Figure 18 shows the distribution of mutual inclinations assuming the flux ratio constraint, a uniform distribution for $\Delta\Omega_{12}$, and the two different priors on α. These distributions are symmetric about $\Delta\phi_{12} = 90°$ because the observables (RV amplitude and potential transits) are invariant under the transformations $i_j \rightarrow i_j + \pi$. The 95% c.l. lower

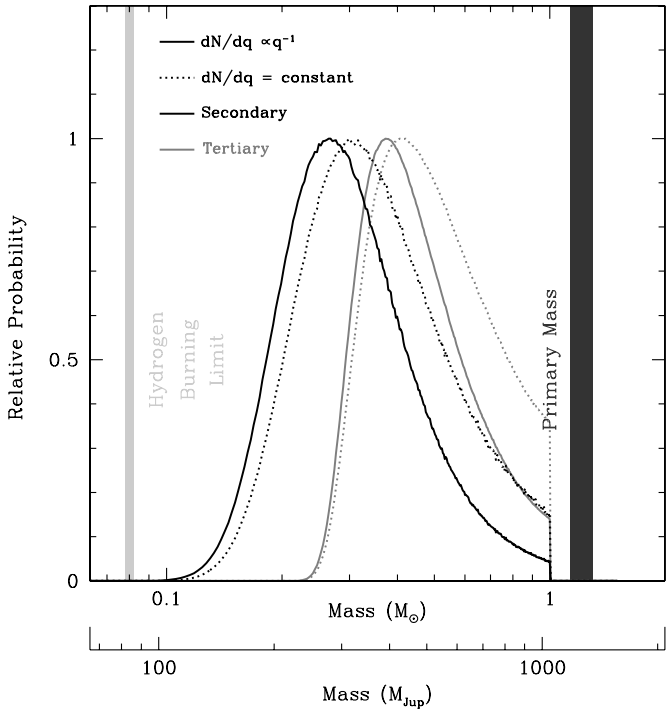

Figure 19. A posteriori probability density for the true masses of the tertiary and secondary. These have been arbitrarily normalized by their peak probability density. The black lines show the probabilities for the secondary assuming the tidal synchronization/coplanarity, for two different priors on the mass ratio q, $dN/dq \propto q^{-1}$ (uniform in $\log q$, solid), and $dN/dq =$ constant (uniform in q, dotted). The gray lines show the probabilities for the tertiary, for the same priors on the mass ratio. In all cases, companion masses $\geqslant 1\,M_{\odot}$ have been excluded.

and upper limits on the true mutual inclinations are 31.°1 and $180^{\circ} - 31.^{\circ}1 = 148.^{\circ}9$ for $\alpha = -1$ and 28.°8 and $180^{\circ} - 28.^{\circ}8 = 151.^{\circ}2$ for $\alpha = 0$. The probability that the mutual inclination is greater than the Kozai angle (Kozai 1962) of 39.°2 or less than the retrograde Kozai angle of 140.°8 is $\sim$ 89% ($\alpha = -1$) and $\sim$85% ($\alpha = 0$).

Figure 19 shows the probability densities of the true mass of the secondary and tertiary, assuming the tidal synchronization/coplanarity and flux ratio constraints, for $\alpha = -1$ and $\alpha = 0$. We infer that the primary and secondary are both likely to be M dwarfs, with the tertiary likely to be somewhat more massive than the secondary.

9. THE KOZAI–LIDOV MECHANISM APPLIED TO TYC 2930

One mechanism of forming short-period binary stars is the Kozai–Lidov mechanism, in which a hierarchical triple system exchanges angular momentum between the inner and outer orbits periodically if the mutual inclination between the inner and outer orbits is $39.^{\circ}2 \lesssim \Delta\phi_{23} \lesssim 141.^{\circ}8$ (Kozai 1962; Lidov 1962). These oscillations drive e_2 to high and low values while decreasing and increasing $\Delta\phi_{23}$, respectively. When combined with tidal friction, these oscillations can cause the semimajor axis of the inner companion (a_2) to decrease, as tidal friction removes energy and circularizes the orbit (Mazeh & Shaham 1979). In addition to short-period binaries in triple systems (Kiseleva et al. 1998; Eggleton & Kiseleva-Eggleton 2001; Tokovinin et al. 2006; Fabrycky & Tremaine 2007), this mechanism has been proposed as an explanation for the prevalence of "Hot Jupiter" gas giant planets with periods of a few days (Wu & Murray 2003; Fabrycky & Tremaine 2007; Wu et al. 2007; Naoz et al. 2011) and the formation of blue straggler stars in globular clusters (Perets & Fabrycky 2009).

To constrain the initial parameters of TYC 2930's progenitor system, we first assume that a_3 and e_3 remain unchanged during the evolution of the system. We can then place an upper limit on the initial a_2 ($a_{2,\mathrm{i}}$) using the stability criteria for triple systems given by (Mardling & Aarseth 2001)

$$\frac{a_3}{a_2} \geqslant C\ f \left[\left(1 + \frac{M_3}{M_1 + M_2}\right) \frac{1 + e_3}{(1 - e_3)^3} \right]^{0.4}, \qquad (10)$$

where $C = 2.8$ is an empirically fit constant and $f = 1 - \frac{0.3}{\pi}\Delta\phi_{23}$ is an ad hoc mutual inclination term. Given the most probable values for the parameters of TYC 2930, and assuming that the initial $\Delta\phi_{23} \sim 90^{\circ}$ such that the Kozai–Lidov mechanism is a significant effect, the initial $a_3/a_2 > 4.4$, and thus the maximum stable a_2 is $a_{2,\mathrm{max}} = 0.96$ AU. To replicate the observed system parameters, we then require $r_{\mathrm{peri}} < 3\,R_1 = r_{\mathrm{tide}}$ for efficient tidal circularization. Generally, the $\cos\Delta\phi_{23}$ required for $r_{\mathrm{peri}} < 3\ R_1$, $\cos\Delta\phi_{23_{\mathrm{crit}}}$, is given by

$$\cos\Delta\phi_{23_{\mathrm{crit}}} = \left(\frac{3}{5}\left[1 - \left(1 - \frac{r_{\mathrm{tide}}}{a_{2,\mathrm{i}}}\right)^2\right]\right)^{1/2} \sim \left(\frac{6\,r_{\mathrm{tide}}}{5\,a_{2,\mathrm{i}}}\right)^{1/2}. \qquad (11)$$

Thus if $a_{2,\mathrm{i}} = 0.3$ AU then $\cos\Delta\phi_{23_{\mathrm{crit}}} \sim 0.25$.

To simulate the Kozai–Lidov mechanism, we use a modified version of the N-body code FEWBODY[25] (Fregeau et al. 2004). In Figure 20, we show an example triple system which has initial parameters consistent with the constraints placed on the progenitor system of TYC 2930: $M_1 = 1.21\,M_{\odot}$, $M_2 = 0.34\,M_{\odot}$, $M_3 = 0.48\,M_{\odot}$, $a_{2,\mathrm{i}} = 0.3$ AU, $a_3 = 4.27$ AU, $e_2 = 0.0$, $e_3 = 0.29$, $\omega_2 = 0^{\circ}$, $\omega_3 = 0^{\circ}$, and $\cos\Delta\phi_{23} = 0.1$. The top panels present the evolution of a_2, a_3, and e_3. The middle and bottom panels show the evolution of $\cos\Delta\phi_{23}$ and $1 - e_2$, respectively. In the middle panel, the teal line designates $\cos\Delta\phi_{23} = 0$. In the bottom panel, the red line shows where e_2 is high enough such that the radius of periastron of the inner binary (r_{peri}) is equal to $2\,R_{\odot}$. The example system goes through Kozai–Lidov cycles, bringing $r_{\mathrm{peri}} < 2\,R_{\odot}$. If the effects of tides were included in our calculation, we would expect that a_2 and $\Delta\phi_{23}$ would decrease over many Kozai cycles.

However, the commonly used, quadrupole-order expansion of the three-body Hamiltonian is insufficient to capture the secular dynamics of triple systems under the test particle approximation when e_3 is non-zero (Lithwick & Naoz 2011; Katz et al. 2011; Naoz et al. 2011). The importance of the octupole-order terms relative to the quadrupole-order terms in the doubly averaged three-body Hamiltonian is given by the parameter

$$\epsilon_{\mathrm{oct}} = \left(\frac{M_0 - M_1}{M_0 + M_1}\right)\left(\frac{a_2}{a_3}\right)\frac{e_3}{1 - e_3^2}. \qquad (12)$$

In the limit that ($M_2 \ll M_1, M_3$) and $e_3 \neq 0$, it is possible for the triple system to "flip," i.e., the system exhibits quasi-periodic cycles in $\Delta\phi_{23}$ through 0, and the tertiary passes between prograde and retrograde (Lithwick & Naoz 2011; Katz et al. 2011). These flips occur even for small values of ϵ_{oct} ($\sim 10^{-3}$) in the test particle approximation, as long as the system is sufficiently inclined and the arguments of periastrons are chosen

[25] FEWBODY is now available at http://fewbody.sourceforge.net/ .

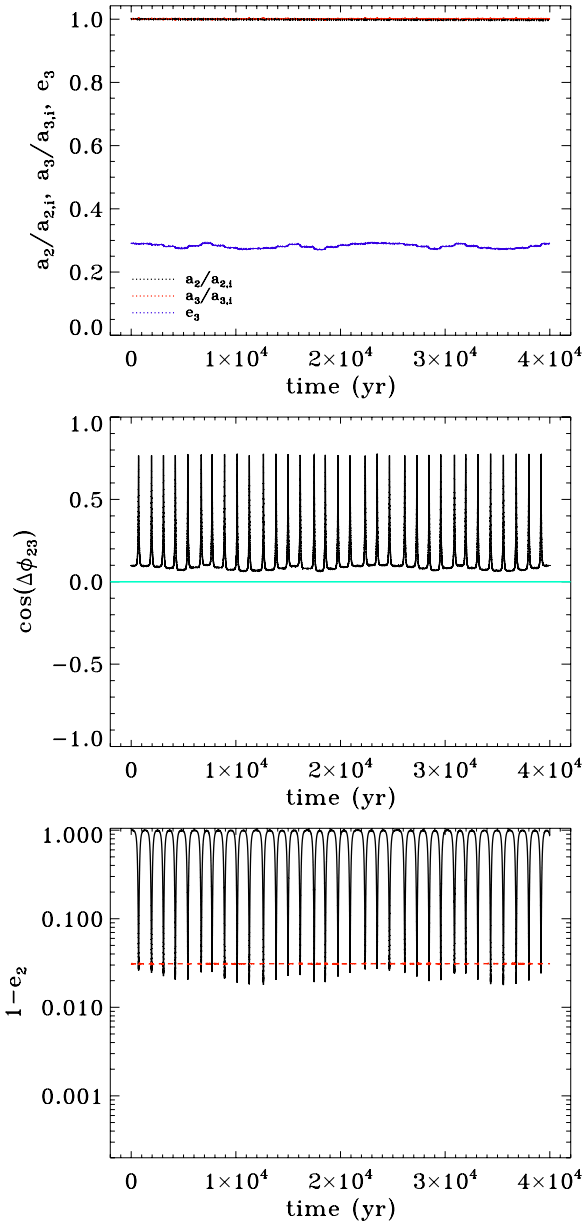

Figure 20. Example of the normal Kozai–Lidov mechanism using parameters consistent with those of TYC 2930's progenitor system. Top: evolution of a_2 (dotted black), a_3 (red dotted), and e_3 (blue dotted). Middle: time evolution of $\cos\Delta\phi_{23}$. The teal line designates $\cos\Delta\phi_{23} = 0$. Bottom: time evolution of e_2 and the red line denotes $r_{\rm peri} < 2\ R_\odot$. Integrations after the first eccentricity maximum are for illustration purposes only, since we do not include the effects of tides here.

(A color version of this figure is available in the online journal.)

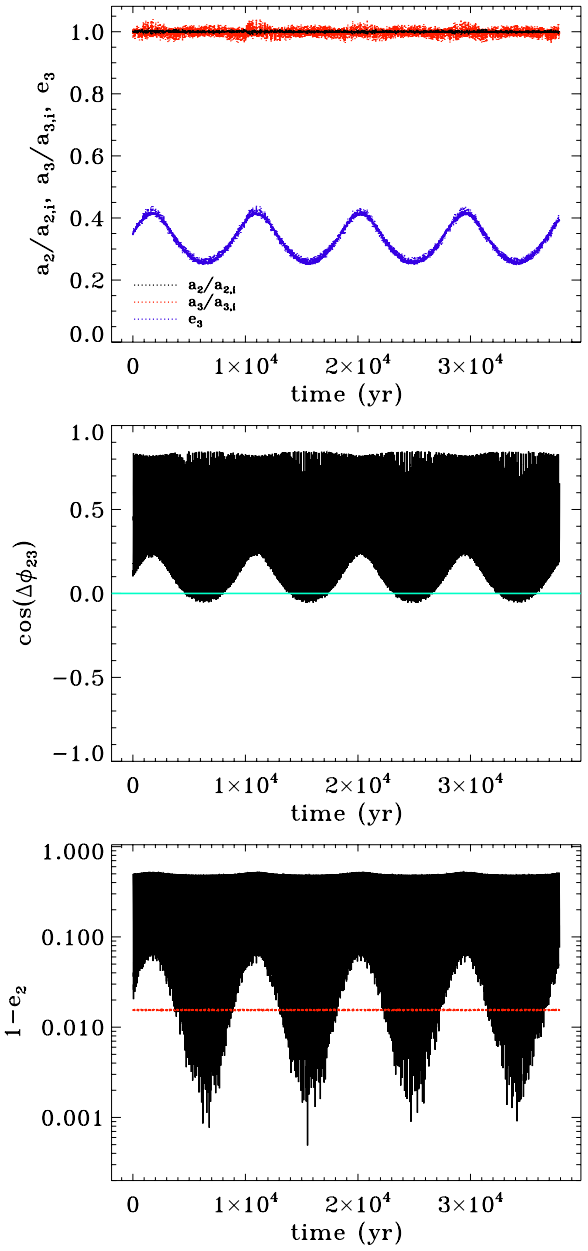

Figure 21. Similar to Figure 20, but for the eccentric Kozai–Lidov mechanism. Note the qualitative differences between the two cases: the changing sign of $\cos\Delta\phi_{23}$ and the extreme eccentricity spikes.

(A color version of this figure is available in the online journal.)

judiciously (see Figures 3 and 7 of Katz et al. 2011; Lithwick & Naoz 2011, respectively).

Flips become increasingly common for triple systems with larger values of $\epsilon_{\rm oct}$, and they correspond to extremely large spikes in e_2, such that $(1 - e_2) \sim 10^{-5}$. Such qualitative behaviors (flips and eccentricity spikes) are referred to as the "eccentric Kozai–Lidov mechanism" and can occur over a broad range of parameters within octupole-order calculations. Shappee & Thompson (2012) have recently highlighted the mass dependence of the eccentric Kozai–Lidov mechanism and performed one of the first explorations of the eccentric Kozai–Lidov mechanism for triple stellar systems. They found that many triple systems become tidally affected while on the main sequence as a result of this mechanism. The mechanism can even be effective for triple systems that would not otherwise become tidally affected during normal Kozai–Lidov oscillations in quadrupole-order calculations.

As an example of the eccentric Kozai–Lidov mechanism, we integrated the orbit of a system with $M_1 = 1.21\,M_\odot$, $M_2 = 0.34\,M_\odot$, $M_3 = 0.48\,M_\odot$, $a_2 = 0.6$ AU, $a_3 = 4.27$ AU, $e_2 = 0.5$, $e_3 = 0.35$, $\omega_2 = 0°$, $\omega_3 = 262°$, and $\cos\Delta\phi_{23} = 0.1$. Figure 21 shows the resulting evolution. There are many qualitative differences between the evolution of this system and that shown in Figure 20. The most obvious of these are the periodic oscillations of e_3, the long-term oscillations of the minimum $\cos\Delta\phi_{23}$, and the flipping of the sign of $\cos\Delta\phi_{23}$, which corresponds to large spikes in $e_2 \sim 0.9995$.

What is the fate of systems that become tidally affected due to the eccentric Kozai–Lidov mechanism? Unfortunately, no study

has been performed to investigate the eccentric Kozai–Lidov mechanism with the inclusion of tidal dissipation for triple stellar systems. It is possible that tidal friction will simply detune the eccentric Kozai–Lidov mechanism, inhibiting the extreme spikes in eccentricity observed in our example system. However, Naoz et al. (2011) investigated the eccentric Kozai–Lidov mechanism with tidal friction for a Jupiter-mass secondary in an octupole-order calculation. They demonstrate that the extremely high e_2 obtained during a flip can lead to large tidal effects, which rapidly capture the planet in a short-period retrograde orbit. They coin this mechanism "Kozai capture" and claim it may explain the occurrence of retrograde, short-period, gas giant planets. A similar mechanism may operate for stellar triple systems, in which Kozai capture would cause a rapid dissipation of orbital energy from the inner binary during its evolution. This would result in a circularized inner binary with a semimajor axis of a few $r_{\rm peri}$, and thus provides a plausible scenario by which TYC 2930's secondary star was driven to such a small semimajor axis.

10. CONCLUSION

We have discovered a short-period companion to TYC 2930-00872-1 with a minimum mass below the hydrogen-burning limit. Despite its relatively high transit probability, we exclude any transits of the companion with high confidence using data from three ground-based telescopes. A long-term trend in the RVs indicates the presence of a longer-period tertiary in the system. The tertiary's spectral lines are not detected in our spectroscopic data, its fluxes do not significantly contribute to our SED fitting, and direct imaging excludes stellar-mass, main-sequence companions out to projected separations of 30 AU. Our spectra show the clear presence of Ca H and K core emission, but there is an unexpected lack of photometric variability, and the measured $v \sin I$ is significantly smaller than expected if the primary's rotation rate was tidally synchronized to the inner companion's orbital period. This suggests the primary's stellar spin axis is closely aligned to the line of sight. Given the age of the system, it is expected that the inner companion's orbital angular momentum vector is aligned with the stellar spin axis; therefore its line-of-sight orbital inclination is low, and its true mass is likely to be stellar. The absence of any detected signal from either component in the spectra and SED place an upper mass limit of $\sim 1.0\,M_{\odot}$, if they are not stellar remnants. Assuming the tertiary is not a remnant, the upper mass limit places a lower limit to its line-of-sight inclination, which results in a significant mutual inclination between the secondary and tertiary. Such mutual inclinations are expected if the system's dynamical history was driven by the Kozai–Lidov mechanism. Long-term RV monitoring of the outer companion to obtain reliable orbital parameters will greatly improve the constraints that can be placed on the mutual inclination between the secondary and tertiary. Furthermore, high signal-to-noise ratio spectroscopic observations that could detect the presence of the (presumably) M dwarf companions would also allow for masses to be assigned to both objects and improve the inclination constraints.

K.S., L.H., and J.P. acknowledge funding support from the Vanderbilt Initiative in Data-Intensive Astrophysics (VIDA) from Vanderbilt University and from NSF Career Award AST-0349075. E.A. thanks the NSF for Career Grant AST-0645416. J.W. acknowledges support from NSF Astronomy and Astrophysics Postdoctoral Fellowship AST 08-02230. L.G. acknowledges financial support provided by the PAPDRJ CAPES/FAPERJ Fellowship. L.D.-F. acknowledges financial support provided by CAPES and ESO student fellowship. G.F.P.d.M. acknowledges financial support from CNPq grant Nos. 476909/2006-6 and 474972/2009-7, plus a FAPERJ grant No. APQ1/26/170.687/2004. C.V. and G.W. acknowledge support from the Pennsylvania Space Grant Consortium. Operation of Allegheny Observatory is supported in part by the Theiss Memorial Endowment. Work by B.S.G. and T.B. was partially supported by NSF Career Grant AST-1056524. We thank J. Fregeau for making the code FEWBODY publicly available. This work is supported in part by an Alfred P. Sloan Foundation Fellowship and NSF Grant AST-0908816. B.S. was supported by a Graduate Research Fellowship from the National Science Foundation.

This work was partially supported by funding from the Center for Exoplanets and Habitable Worlds. The Center for Exoplanets and Habitable Worlds is supported by the Pennsylvania State University, the Eberly College of Science, and the Pennsylvania Space Grant Consortium. This research has made use of the SIMBAD database, operated at CDS, Strasbourg, France. This publication makes use of data products from the Two Micron All Sky Survey, which is a joint project of the University of Massachusetts and the Infrared Processing and Analysis Center/California Institute of Technology, funded by the National Aeronautics and Space Administration and the National Science Foundation. This publication makes use of data products from the *Wide-field Infrared Survey Explorer*, which is a joint project of the University of California, Los Angeles, and the Jet Propulsion Laboratory/California Institute of Technology, funded by the National Aeronautics and Space Administration.

Funding for the MARVELS multi-object Doppler instrument was provided by the W. M. Keck Foundation and NSF with grant AST-0705139. The MARVELS survey was partially funded by the SDSS-III consortium, NSF Grant AST-0705139, NASA with grant NNX07AP14G and the University of Florida. This work has made use of observations taken with the Telescopio Nationale Galileo (TNG) operated on the island of La Palma by the Fundation Galileo Galilei, funded by the Instituto Nazionale di Astrofisica (INAF), in the Spanish *Observatorio del Roque de los Muchachos* of the Instituto de Astrofísica de Canarias (IAC).

This work was based on observations with the SDSS 2.5 m telescope. Funding for SDSS-III has been provided by the Alfred P. Sloan Foundation, the Participating Institutions, the National Science Foundation, and the U.S. Department of Energy Office of Science. The SDSS-III Web site is http://www.sdss3.org/. SDSS-III is managed by the Astrophysical Research Consortium for the Participating Institutions of the SDSS-III Collaboration including the University of Arizona, the Brazilian Participation Group, Brookhaven National Laboratory, University of Cambridge, Carnegie Mellon University, University of Florida, the French Participation Group, the German Participation Group, Harvard University, the Instituto de Astrofisica de Canarias, the Michigan State/Notre Dame/JINA Participation Group, Johns Hopkins University, Lawrence Berkeley National Laboratory, Max Planck Institute for Astrophysics, Max-Planck-Institute for Extraterrestrial Physics, New Mexico State University, New York University, Ohio State University, Pennsylvania State University, University of Portsmouth, Princeton University, the Spanish Participation Group, University of Tokyo, University of Utah, Vanderbilt University, University of Virginia, University of Washington, and Yale University.

REFERENCES

Alard, C., & Lupton, R. H. 1998, ApJ, 503, 325
Baraffe, I., Chabrier, G., Allard, F., & Hauschildt, P. H. 1998, A&A, 337, 403
Baraffe, I., Chabrier, G., Barman, T. S., Allard, F., & Hauschildt, P. H. 2003, A&A, 402, 701
Barnes, R., Mullins, K., Goldblatt, C., et al. 2012, Astrobiology, submitted (arXiv:1203.5104)
Bensby, T., Feltzing, S., & Lundström, I. 2003, A&A, 410, 527
Burke, C. J., Gaudi, B. S., DePoy, D. L., & Pogge, R. W. 2006, AJ, 132, 210
Claret, A., & Hauschildt, P. H. 2003, A&A, 412, 241
Collier Cameron, A., Wilson, D. M., West, R. G., et al. 2007, MNRAS, 380, 1230
Counselman, C. C., III. 1973, ApJ, 180, 307
Demarque, P., Woo, J.-H., Kim, Y.-C., & Yi, S. K. 2004, ApJS, 155, 667
Duncan, D. K., Vaughan, A. H., Wilson, O. C., et al. 1991, ApJS, 76, 383
Eggleton, P. P., & Kiseleva-Eggleton, L. 2001, ApJ, 562, 1012
Eisenstein, D. J., Weinberg, D. H., Agol, E., et al. 2011, AJ, 142, 72
Erskine, D. J. 2002, PASP, 115, 255
Erskine, D. J., Edelstein, J., Feuerstein, W. M., & Welsh, B. 2003, ApJ, 592, 103
Fabrycky, D., & Tremaine, S. 2007, ApJ, 669, 1298
Femenía, B., Rebolo, R., Pérez-Prieto, J. A., et al. 2011, MNRAS, 413, 1524
Ferraz-Mello, S., Rodríguez, A., & Hussmann, H. 2008, Celest. Mech. Dyn. Astron., 101, 171
Fleming, S. W., Ge, J., Mahadevan, S., et al. 2010, ApJ, 718, 1186
Ford, E. B. 2006, ApJ, 642, 505
Fregeau, J. M., Cheung, P., Portegies Zwart, S. F., & Rasio, F. A. 2004, MNRAS, 352, 1
Fried, D. L. 1978, J. Opt. Soc. Am., 68, 1651
Ge, J. 2002, ApJ, 571, L165
Ge, J., Erskine, D. J., & Rushford, M. 2002, PASP, 114, 1016
Ge, J., Mahadevan, S., Lee, B., et al. 2008, in ASP Conf. Ser. 398, Extreme Solar Systems, ed. D. Fischer, F. A. Rasio, S. E. Thorsett, & A. Wolszczan (San Francisco, CA: ASP), 449
Gelman, A., Carlin, J. B., Stern, H. S., & Rubin, D. B. 2003, Bayesian Data Analysis (New York: Chapman and Hall)
Ghez, A. M., Salim, S., Weinberg, N. N., et al. 2008, ApJ, 689, 1044
Ghezzi, L., Cunha, K., Smith, V. V., et al. 2010, ApJ, 720, 1290
Girardi, L., Bertelli, G., Bressan, A., et al. 2002, A&A, 391, 195
Goldreich, P., & Soter, S. 1966, Icarus, 5, 375
Gómez Maqueo Chew, Y., Stassun, K. G., Prša, A., et al. 2012, ApJ, 745, 58
Gratton, R. G., Bonanno, G., Bruno, P., et al. 2001, Exp. Astron., 12, 107
Griffin, R., & Griffin, R. 1973, MNRAS, 162, 255
Gunn, J. E., Siegmund, W. A., Mannery, E. J., et al. 2006, AJ, 131, 2332
Hartman, J. D., Gaudi, B. S., Pinsonneault, M. H., et al. 2009, ApJ, 691, 342
Hauschildt, P. H., Allard, F., & Baron, E. 1999, ApJ, 512, 377
Heggie, D. C. 1975, MNRAS, 173, 729
Høg, E., Fabricius, C., Makarov, V. V., et al. 2000, A&A, 355L, 27
Kane, S. R., & von Braun, K. 2008, ApJ, 689, 492
Katz, B., Dong, S., & Malhotra, R. 2011, Phys. Rev. Lett., 107, 181101
Kaufer, A., Stahl, O., Tubbesing, S., et al. 1999, Messenger, 95, 8
Khaliullin, K. F., & Khaliullina, A. I. 2011, MNRAS, 411, 2804
Kiseleva, L. G., Eggleton, P. P., & Mikkola, S. 1998, MNRAS, 300, 292
Kozai, Y. 1962, AJ, 67, 591
Kurucz, R. 1993, ATLAS9 Stellar Atmosphere Programs and 2 km/s Grid, Kurucz CD-ROM No. 13 (Cambridge, MA: Smithsonian Astrophysical Observatory), 13
Landolt, A. U. 2009, AJ, 137, 4186
Landolt, A. U., & Uomoto, A. K. 2007, AJ, 133, 768
Lee, B. L., Ge, J., Fleming, S. W., et al. 2011, ApJ, 728, 32
Lidov, M. L. 1962, Planet. Space Sci., 9, 719
Lin, D. N. C., Bodenheimer, P., & Richardson, D. C. 1996, Nature, 380, 606
Lithwick, Y., & Naoz, S. 2011, ApJ, 742, 94
Lovis, C., Dumusque, X., Santos, N. C., et al. 2011, arXiv:1107.5325
Mamajek, E. E., & Hillenbrand, L. A. 2008, ApJ, 687, 1264
Mandel, K., & Agol, E. 2002, ApJ, 580, L171
Marcy, G. W., & Butler, R. P. 1992, PASP, 104, 270
Mardling, R. A., & Aarseth, S. J. 2001, MNRAS, 321, 398
Martin, D. C., Fanson, J., Schiminovich, D., et al. 2005, ApJ, 619, 1
Matsumura, S., Takeda, G., & Rasio, F. A. 2008, ApJ, 686, L29
Mazeh, T., & Shaham, J. 1979, A&A, 77, 145
Naoz, S., Farr, W. M., Lithwick, Y., Rasio, F. A., & Teyssandier, J. 2011, Nature, 473, 187
Noyes, R. W., Hartmann, L. W., Baliunas, S. L., Duncan, D. K., & Vaughan, A. H. 1984, ApJ, 279, 763
Oscoz, A., Rebolo, R., López, R., et al. 2008, Proc. SPIE, 7014, 701447
Pepper, J., Pogge, R. W., DePoy, D. L., et al. 2007, PASP, 119, 92
Perets, H. B., & Fabrycky, D. C. 2009, ApJ, 697, 1048
Pfahl, E., Arras, P., & Paxton, B. 2008, ApJ, 679, 783
Pollacco, D. L., Skillen, I., Collier Cameron, A., et al. 2006, PASP, 118, 1407
Raghavan, D., McAlister, H. A., Henry, T. J., et al. 2010, ApJS, 190, 1
Ramsey, L. W., Adams, M. T., Barnes, T. G., et al. 1998, Proc. SPIE, 3352, 34
Schlegel, D. J., Finkbeiner, D. P., & Davis, M. 1998, ApJ, 500, 525
Shappee, B. J., & Thompson, T. A. 2012, arXiv:1204.1053
Shetrone, M., Cornell, M. E., Fowler, J. R., et al. 2007, PASP, 119, 556
Siverd, R. J., Pepper, J., Stanek, K., et al. 2009, in Proc. IAU Symp. 253, Transiting Planets, ed. F. Pont, D. D. Sasselov, & M. J. Holman (Cambridge: Cambridge Univ. Press), 350
Skrutskie, M. F., Cutri, R. M., Stiening, R., et al. 2006, AJ, 131, 1163
Sterzik, M. F., & Tokovinin, A. A. 2002, A&A, 384, 1030
Stetson, P. B. 1987, PASP, 99, 191
Tokovinin, A. 2008, MNRAS, 389, 925
Tokovinin, A., Thomas, S., Sterzik, M., & Udry, S. 2006, A&A, 450, 681
Torres, G., Andersen, J., & Giménez, A. 2010, A&AR, 18, 67
Tull, R. G. 1998, Proc. SPIE, 3355, 387
van Eyken, J. C., Ge, J., & Mahadevan, S. 2011, ApJS, 189, 156
van Leeuwen, F. 2007, A&A, 474, 653
Vaughan, A. H., & Preston, G. W. 1980, PASP, 92, 385
Vaughan, A. H., Preston, G. W., & Wilson, O. C. 1978, PASP, 90, 267
Wang, J., Ge, J., Wan, X., Lee, B., & De Lee, N. 2012, PASP, 124, 598
Wang, S., Hildebrand, R. H., Hobbs, L. M., et al. 2003, Proc. SPIE, 4841, 1145
Wisniewski, J. P., Ge, J., Crepp, J. R., et al. 2012, AJ, 143, 107
Wright, E. L., Eisenhardt, P. R. M., Mainzer, A. K., et al. 2010, AJ, 140, 1868
Wright, J. T., & Howard, A. W. 2009, ApJS, 182, 205
Wu, Y., & Murray, N. 2003, ApJ, 589, 605
Wu, Y., Murray, N. W., & Ramsahai, J. M. 2007, ApJ, 670, 820
Zahn, J.-P., & Bouchet, L. 1989, A&A, 223, 112
Zakamska, N. L., Pan, M., & Ford, E. B. 2011, MNRAS, 410, 1895